Master's thesis

NTNU
Norwegian University of Science and Technology
Faculty of Natural Sciences
Department of Physics

Konstanse Kvalem Seljelid

CO_2 Capture and Storage in Fluorohectorite Clay

Role of Pressure, Temperature and Interlayer Cation: XRD Studies

Master's thesis in Physics
Supervisor: Jon Otto Fossum
May 2019

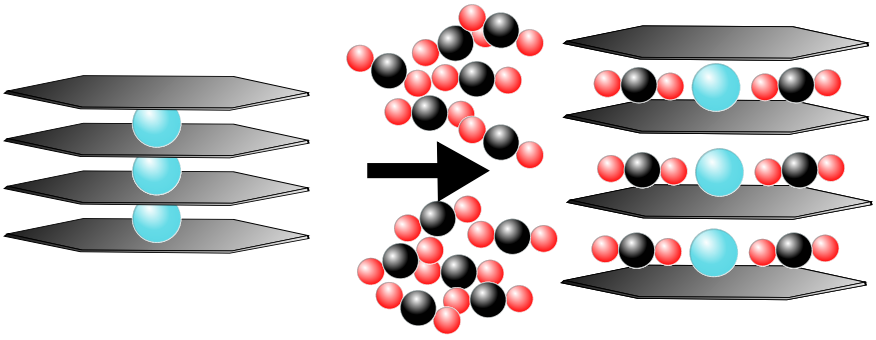

Konstanse Kvalem Seljelid

NTNU
Norwegian University of
Science and Technology

Konstanse Kvalem Seljelid

CO_2 Capture and Storage in Fluorohectorite Clay

Role of Pressure, Temperature and Interlayer Cation: XRD Studies

Master's thesis in Physics
Supervisor: Jon Otto Fossum
May 2019

Norwegian University of Science and Technology
Faculty of Natural Sciences
Department of Physics

NTNU
Norwegian University of
Science and Technology

Preface

This thesis concludes the last year of my Master's Degree of Physics. The experiments have been carried out at the European Synchrotron Radiation Facility and the Brazilian Synchrotron Light Laboratory. The main part of the work, namely the analysis, was performed at the Norwegian University of Science and Technology (NTNU), at the Soft and Complex Matter Group.

Our group has been working with clay, its properties and possible applications for a long time. Previous studies concern the swelling of smectite clay in contact with water. However, due to the pressing problematic of increasing emission of anthropogenic CO_2, investigations into whether the swelling clay could also be utilized in CO_2 capture and storage have been initiated. It is in this context my work on CO_2 absorption in fluorohectorite clay is motivated, and the results are encouraging for further investigations into this field of study.

I am grateful for the experience I have gained during these two years at NTNU, and would like to thank my supervisor, Prof. Jon Otto Fossum for providing me with unique opportunities. Conducting experiments at two synchrotron facilities, as well as attending workshops and the Geilo School has been very educational. It has also been very inspiring to meet talented and passionate scientists presenting their work.

I would also like to thank Kristoffer W.B. Hunvik, who, in practice, has acted as my co-supervisor, and aided me in minor as well as major issues. It is greatly appreciated. My thanks also goes to Kenneth D. Knudsen and Barbara Pacáková for good guidance during the data analysis.

To my colleagues, friends and family: Your encouragements, positive attitude, countless coffee breaks and numerous dances have been crucial for quenching my frustrations and making good days better. Thank you for your patience!

Lastly, I acknowledge the European Synchrotron Radiation Facility for provision of synchrotron radiation facilities and would like to thank Dmitry Chernyshov, Vadim Diadkin and Wouter Van Beek for assistance in using beamline BM01.

This research also used resources of the Brazilian Synchrotron Light Laboratory (LNLS), an open national facility operated by the Brazilian Centre for Research in Energy and Materials (CNPEM) for the Brazilian Ministry for Science, Technology, Innovations and Communications (MCTIC). Antonio Augusto Malfatti Gasperiniis and the rest of the beamline staff are acknowledged for the assistance during the experiments at the beamline XRD2.

Abstract

Addressing the growing issue of CO_2 emission into the atmosphere, different technologies within Carbon Capture and Storage are being investigated. Clay minerals are likewise studied in this context due to their ability to absorb CO_2, in addition to being cheap and environmental friendly. In this work, CO_2 intercalation and retention in synthetic fluorohectorite clay has been studied through powder X-ray diffraction (XRD) at two synchrotron facilities. Additionally, the role of the charge compensating cations on the intercalation was probed. The cations used were Ni^{2+}, Li^{+}, Na^{+}, Ba^{2+}, Cs^{+} and Ca^{2+}

A custom sample cell allowed the use of glass capillaries during measurements with pressurized CO_2, where the highest pressure applied was 50 bar. Temperature was controlled through a cryojet directed at the capillary, and was between 203 K and 423 K.

The results reveal that NiFh, LiFh and NaFh absorb CO_2. For NiFh the critical pressure inducing a transition from dry NiFh to one layer of CO_2 intercalated was observed to be 12 bar at a temperature of 300 K. However, the final basal spacing of 12.29 Å was not achieved until pressure reached 40 bar. Similarly, an experiment was performed keeping the pressure constant at 1 bar while reducing the temperature. This displayed initiation of a transition in NiFh at 233 K. Full intercalation with a basal spacing of 12.32 Å was reached at 213 K. The retention properties were investigated by heating the sample, and CO_2 release was observed at 263 K. The corresponding values for LiFh are 20 bar and 253 K for intercalation, while the release was induced at 268 K and 1 bar and completed at 343 K and 1 bar. NaFh intercalated CO_2 at 20 bar and 253 K, but no release experiment was performed on this sample.

In conclusion this investigation has determined the conditions for intercalation and retention of CO_2 in NiFh and LiFh. Intercalation was found to be quite rapid ($\sim$ min) once the energy barrier was breached. For NaFh there was also observed signs of intercalation, showing that intercalation dynamics strongly depend on the interlayer cation. Intercalation of CO_2 into clays such as NiFh and LiFh is promising for use in carbon capture and storage technology. Especially interesting is the utilization of clays as adsorbents in industry. Also increased capacity for CO_2 storage in geological sites is beneficial.

Samandrag

Som konsekvens av aukande CO_2 utslepp i atmosfæren vert fleire teknologiar innanfor karbonfangst og lagring undersøkt. I denne samanhengen vert også leiremineral studert på grunn av deira evner til å absorbere CO_2, i tillegg til å vere billeg og miljøvenleg. I dette arbeidet har absorpsjon og retensjons eigenskapane til den syntetiske leira fluor-hektoritt vorte studert med røntgendiffraksjon på to synkrotron fasilitetar. I tillegg har rolla til dei ladningskompenserande kationa i absorpsjonen vorte undersøkt. Kationa som vart brukt var Ni^{2+}, Li^{+}, Na^{+}, Ba^{2+}, Cs^{+} og Ca^{2+}.

Ei spesiallaga prøvecelle mogleggjorde bruken av glaskapillarar i målingar med trykksatt CO_2, der det høgaste trykket var 50 bar. Temperaturen vart kontrollert med ein kryo-jet retta mot kapillaren, og var mellom 203 K og 423 K.

Resultata visar at pulvera NiFh, LiFh og NaFh absorberer CO_2. Det kritiske trykket for NiFh som set i gang ein overgang frå tørr NiFh til eit lag med CO_2 mellom leirelaga, vart observert til å vere 12 bar ved 300 K. Den endelege basale avstanden på 12.29 Å vart derimot ikkje nådd før trykket vart 40 bar. Likeeins vart eit anna eksperiment utført kor trykket vart halde konstant på 1 bar samstundes som temperaturen vart senka. Her vart overgangen for NiFh observert ved 233 K. Full absorpsjon med ein basal avstand på 12.32 Å vart nådd ved 213 K. Retensjonseigenskapane vart undersøkt ved oppvarming av prøva, og NiFh heldt på karbondioksida til 263 K. Tilsvarande verdiar for LiFh er 20 bar og 253 K for absorpsjon, medan frigjevinga av CO_2 vart utløyst ved 268 K og 1 bar, og fullført ved 343 K og 1 bar. NaFh absorberte CO_2 ved eit trykk på 20 bar og ein temperatur på 253 K, men ingen oppvarming vart utført for denne prøven.

Desse undersøkingane har bestemt vilkåra for absorpsjon og retensjon av CO_2 i NiFh og LiFh. Undersøkingane har også demonstrert at absorpsjonen er hurtig ($\sim$ min) etter energibarriera er passert. NaFh visar også teikn til å absorbere CO_2, noko som indikerer at absorbasjonen er sterkt avhengig av det ladningskompenserande kationet. Absorbasjon av CO_2 i leirer som NiFh og LiFh er lovande i samanheng med karbonfangst og lagringsteknologi. Spesielt interessant er bruken av leire som adsorberande materiale i industrien. I tillegg er auka lagringskapasitet i geologiske formasjonar fordelaktig.

Contents

Preface **i**

Abstract **iii**

Samandrag **v**

List of Figures **x**

List of Tables **x**

Abbreviations **xi**

1 Introduction **1**

2 Theory **3**

2.1 Clay minerals . . . 3

2.1.1 Structure . . . 3

2.1.2 Interlayer cation and swelling . . . 6

2.1.3 Fluorohectorite . . . 6

2.2 X-ray diffraction . . . 7

2.2.1 Bragg's law . . . 7

2.2.2 Reciprocal space and Laue's diffraction condition . . . 8

2.2.3 Ewald sphere . . . 11

2.2.4 Relating the *hkl* plane to the reciprocal lattice vector . . . 12

2.2.5 Contributions to the diffracted intensity . . . 13

3 Experimental section **17**

3.1 Synchrotron radiation . . . 17

3.2 Experimental setup at ESRF . . . 18

3.3 Experimental setup at LNLS . . . 21

4 Data acquisition and handling **23**

4.1 Calibration . . . 23
4.2 Corrections . . . 23
4.3 Transforming 2D images to 1D data sets . . . 24
4.4 Data extraction . . . 24

5 Results **27**

5.1 Results from ESRF . . . 27
5.1.1 NiFh at 300 K exposed to 0 - 40 bar CO_2 . . . 27
5.1.2 NiFh cooled from 300 K to 203 K at 1 bar . . . 30
5.1.3 NiFh heated from 203 K to 400 K at 1 bar . . . 32
5.1.4 NiFh exposed to 0 - 26 bar at 253 K . . . 34
5.1.5 NiFh exposed to CO_2 in liquid phase . . . 36
5.1.6 NiFh at 13 bar heated from 223 K to 423 K . . . 37
5.2 Results from LNLS . . . 40
5.2.1 Lithium-fluorohectorite . . . 41
5.2.2 Sodium-fluorohectorite . . . 42
5.2.3 Barium-fluorohectorite . . . 43
5.2.4 Cesium-fluorohectorite . . . 44
5.2.5 Calcium-fluorohectorite . . . 44

6 Discussion **47**

6.1 Nickel-fluorohectorite . . . 47
6.2 Lithium-fluorohectorite . . . 50
6.3 Effect of cation size and charge on the intercalation of CO_2 . . . 50

7 Conclusion **53**

7.1 Concluding remarks . . . 53
7.2 Further studies and outlook . . . 53

A Calcium-fluorohectorite **55**

References **57**

List of Figures

2.1 Clay particle. . . . 4
2.2 1:1 and 2:1 layer structure of clay minerals. . . . 5
2.3 Bragg's law. . . . 7
2.4 2D lattice with primitive translation vectors. . . . 8
2.5 Miller plane. . . . 9
2.6 Laue diffraction condition. . . . 10
2.7 The Ewald sphere. . . . 11
2.8 Ewald sphere for a powder. . . . 12
2.9 Plane intersecting crystallographic axes. . . . 13
3.1 General setup of a synchrotron. . . . 18
3.2 Experimental setup at ESRF. . . . 19
3.3 High pressure sample cell. . . . 20
3.4 Experimental setup at LNLS. . . . 21
4.1 Example diffraction image and integrated image. . . . 24
5.1 Integrated diffractogram of NiFh exposed to 0 to 40 bar as a function of q. . . . 28
5.2 NiFh exposed to increasing pressure at 300 K. . . . 29
5.3 Integrated diffractogram of NiFh cooled to 253 K as a function of q. . . . 30
5.4 NiFh cooled to 253 K at 1 bar. . . . 31
5.5 Integrated diffractogram of NiFh heated from 203 K as a function of q. . . . 32
5.6 NiFh heated from 203 K to 400 K at 1 bar. . . . 33
5.7 Integrated diffractogram of NiFh exposed to 0 - 26 bar at 253 K as a function of q. . . . 34
5.8 NiFh exposed to 0 - 26 bar at 253 K. . . . 35
5.9 CO_2 phase diagram. . . . 36
5.10 NiFh exposed to CO_2 in liquid phase. . . . 37
5.11 Integrated diffractogram of NiFh at 13 bar heated from 223 K as a function of q. . . . 37
5.12 NiFh at 13 bar heated from 223 K to 423 K. . . . 38
5.13 Ionic radii of ions. . . . 40

5.14 LiFh exposed to different pressures at 253 K. 41
5.15 LiFh heated from 253 K to 403 K at 1 bar. 42
5.16 NaFh exposed to increasing pressure at 253 K. 42
5.17 BaFh exposed to different pressures and temperatures. 43
5.18 CsFh exposed to different pressures at 253 K. 44
5.19 CaFh exposed to increasing pressure at 253 K. 45
A.1 CaFh heated from 253 K to 353 K at 1 bar. 55

List of Tables

1 Technical information about the experiment at ESRF. 19
2 Technical information about the experiment at LNLS. 21
3 Basal spacings of clays. 45

List of abbreviations

BaFh	Barium-fluorohectorite
CaFh	Calcium-fluorohectorite
CCS	Carbon Capture and Storage
CFC	Chloro- Fluorocarbon
CO_2	Carbon dioxide
CsFh	Cesium-fluorohectorite
ESRF	European Synchrotron Radiation Facility
GHG	Green House Gas
LiFh	Lithium-fluorohectorite
LNLS	Laboratório Nacional de Luz Síncrotron
NaFh	Sodium-fluorohectorite
NiFh	Nickel-fluorohectorite
NMR	Nuclear Magnetic Resonance
RF	Radio Frequency
WL	Water Layer
XRD	X-ray diffraction

1 Introduction

The atmosphere is vital for the earth to be habitable. It provides a pressure supporting the existence of liquid water on the surface, and acts as a protective shield against harmful radiation [1, 2]. In addition to this, several greenhouse gases (GHGs) create a blanketing effect by containing part of the heat radiated from the earth after absorption of solar radiation [3], thus maintaining a stable temperature appropriate to sustain life. Despite the importance of the atmosphere, human activity has severely damaged it in recent years. In the late 1970s the concentration of ozone in the atmosphere decreased due to anthropogenic emission of chloro- fluorocarbons (CFCs) destroying the ozone [2]. To prevent further depletion of ozone, an international agreement to reduce and later ban the use of CFCs was established, resulting in the slow recovery of the ozone layer [2]. However, the composition of the atmosphere is once more being altered by human activity. Due to the emission of GHGs, the earths surface temperature is slowly increasing, posing a major threat to life. Consequences related to the global warming is melting of ice producing a significant increase in the sea levels [3], more extreme weather [4, 5], ocean acidification [6, 7] and extinction of species [8].

The greenhouse gas that is most prominent in the debate about global warming is carbon dioxide (CO_2). This is due to the dramatic increase in the emission of this gas since the industrial revolution, giving birth to global warming. Humans are dependent on processes that release CO_2 into the atmosphere, such as electrical power, cement and steel production and transportation [3]. Furthermore, global warming may be viewed as a symptom of an illness that will intensify as the human consumption increase. The combination of increasing population and increased per capita consumption further diminishes the global sustainability, and will impact necessary resources such as food and water [9, 10]. Additionally, deforestation due to increased food production would further enhance the "domino effect" of disastrous events. To reverse the negative development, a behavioral change on a global scale, both in industries and on a personal basis, is needed [9, 11].

Even though global warming might only be "the tip of the iceberg", it is still vital to limit the impact. To reduce the damage, action is taken to moderate the emission of CO_2. In addition, methods aimed at preventing the released CO_2 from entering the atmosphere are being investigated. Carbon Capture and Storage (CCS) [12] is a collection of such methods, and one that has received much attention is the geological storage method. This is of particular interest due to its potential to store huge amounts of captured CO_2 at sites with already existing infrastructure to accommodate this. Geological storage is the storage of CO_2 in formations such as depleted oil or gas reservoirs, unminable coal-beds or saline aquifers [12], able to contain CO_2 for long periods of time. Although geological storage of CO_2 is highly desirable there are many factors to consider [13, 12]. One considerations is the amount of swelling clay minerals present in the rock formation. Large amounts of swelling clay may cause beneficial closure of open pathways and thus hinder escape of e.g CO_2 gas or fluid. The clay also holds an unrealized potential for storing CO_2. On the other hand, the swelling clays could also trigger fractures, opening escape routes for the stored CO_2.

The swelling is a consequence of absorption of molecules such as water or CO_2 into spaces in the clay particles, and it is interesting to study whether these interlayer spaces can be used for storing CO_2. Utilization of this potential would further increase the storage capacity of rock formations, and open up possibilities for using rock formations previously disregarded for CO_2 storage.

In addition to the promising potential of clay in geological storage, it may also be beneficial to use clay in membranes for post-combustion separation of CO_2 at industrial sites [12, 14]. The use of clay fillers in mixed matrix membranes have proven to increase the CO_2 selectivity of the membrane and increase the permeance [14, 15, 16]. Further technological development may prove able to utilize clay as adsorbents, adsorbing CO_2 at emission site and releasing it for transport at a given pressure and temperature conditions [12].

Due to the importance of clay in geological storage sites and its potential in other CO_2 mitigating products, scientists are investigating the interactions of CO_2 and clay. The properties of clay in contact with water have been extensively characterized, and the knowledge gained from this may extended to the field of CO_2

absorption, as these interactions are also important at geological storage sites [17, 18, 19, 20, 21]. Schaef et al. found that interactions with water might even enhance the ability of the clay to absorb CO_2 to a certain extent [22]. Others have observed that even in the absence of water, CO_2 is still able to penetrate the interlayers of the clays [23, 24, 25, 26].

In this thesis the swelling and retention properties of a synthetic clay mineral, fluorohectorite, in response to different pressures of CO_2 and different temperatures are investigated through X-ray diffraction experiments. The first section of the thesis includes the theory, explaining important concepts such as general structure and properties of clay minerals and X-ray diffraction. Secondly, an experimental section containing the experimental setups used in the experiments at two different synchrotron facilities, European Synchrotron Radiation Facility (ESRF) and Laboratório Nacional de Luz Síncrotron (LNLS), is presented. Also the procedure for preparing samples will be described here. The next section considers the data acquisition and handling, such as calibration and corrections applied to the data. The results will then be presented, before the discussion, and lastly a conclusion of the work with the most important findings and suggestions for further work.

2 Theory

This theory section will present what clay minerals are, some applications of them, their structure and some important properties. It will also contain important concepts of X-ray diffraction and scattering theory, such as Bragg's law, reciprocal space, Laue's condition, the Ewald sphere construction and contributions to the scattered intensity.

2.1 Clay minerals

The terms clay minerals and clays are often used interchangeably about materials composed of fine grained minerals that are formable when wet and hardens when fired. However, while clays are naturally occurring the clay minerals may be synthetic and usually refers to a group of layered phyllosilicates [27]. Here the term "clays" will also be used for clay minerals for convenience. If the term is used about the naturally occurring clays, this will be specified.

In modern society the word "clay" is often associated with mud, which has been important for centuries due to its abundance and unique properties. Its uses range from pottery and art, to house construction through bricks and tiles [27]. However, clay minerals, being both inexpensive and environmentally friendly, are more common in everyday-life than most are aware of [27]. Clay minerals are for example widely used in cosmetics such as skin cream, deodorants and eye shadow [28]. The swelling properties of the clay can reduce oiliness of skin and provide the desired consistency of the cosmetic products. Clays are also used to stabilize emulsions, which is important in different industries, such as food, pharmaceutical and oil industry, preventing flocculation and sedimentation in oil, fat and water emulsions [29, 30]. In addition to this, clay minerals are important in soils, where they are responsible for part of the storage of nutrients for plants [31]. Nutrients adsorbed on the surface of the clay minerals are available for uptake by the plants, and are therefore a significant factor in the growth of plants.

Also in oil drilling and recovery the clay minerals play a crucial role. Clays are used as additives in water based drilling fluids to achieve correct rheology and thermal properties [32]. This has an additional benefit, as the clay coats the borehole walls, temporarily protecting from wellbore collapse [33]. However, swelling clays in the rock of the well can also cause problems when drilling, as it may change the properties of the drilling fluid. The clay also affects the stability of the drilling hole, and can cause wellbore collapse if not treated with proper care [34, 35]. Similar challenges to those related to oil recovery also concerns CO_2 storage to some extent, as mentioned in section 1.

Nuclear and chemical waste handling is also reliant on clays as barriers and buffers [36]. Sealed containers of waste are buried deep in the ground and the area around the container is filled with clay. The swelling properties of the clay causes it to absorb water attempting to penetrate the barrier, preventing it from reaching the container. On the other hand, the clay will also absorb the radionuclides in case of a spill, and thus protect the groundwater from pollution. Considering all the different applications of clays and its impact in everyday life, the importance of understanding the different properties of clay minerals and the mechanisms behind becomes apparent.

2.1.1 Structure

The general structure of clays consists of tetrahedral sheets connected to octahedral sheets in a repeating order. In general the composition of the tetrahedron is with oxygen at the corners and a silicon cation at the center, thus having the chemical formula SiO_4. Figure 2.1e) shows how the connected tetrahedrons share their corner oxygen atoms, creating a hexagonal basal layer of oxygen. It can also be seen from the figure

that all the apical oxygen atoms point in the same direction, joining the tetrahedral sheet to the octahedral sheet. The octahedra contain one cation coordinated to six oxygen atoms or hydroxyl ions (OH^{-1}) and share the edges to make up the octahedral sheet [37].

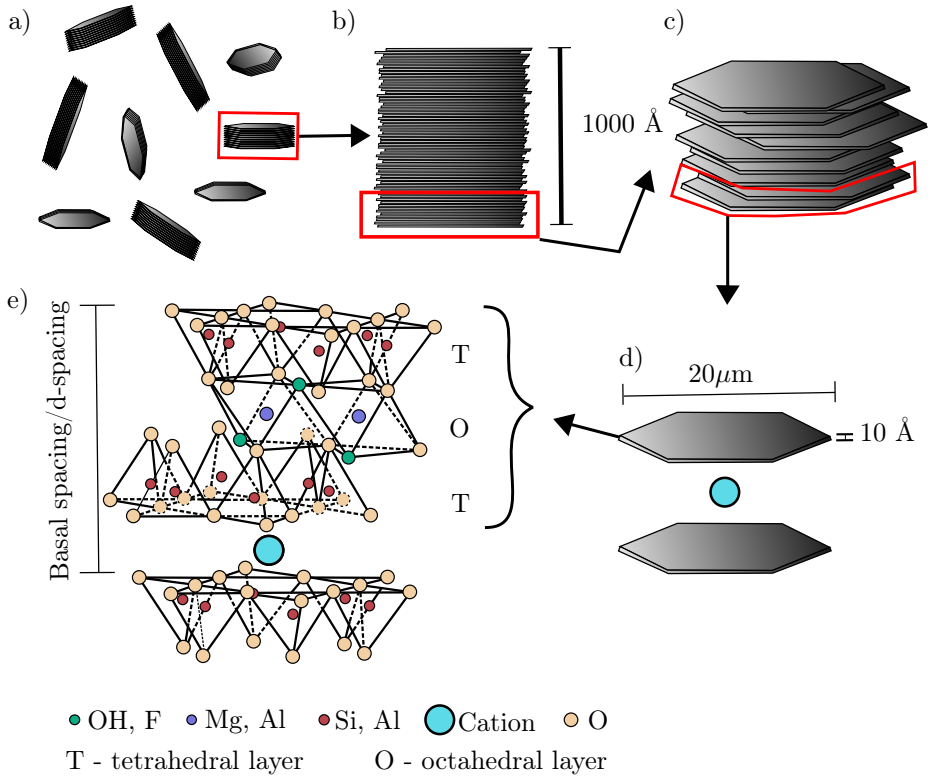

Figure 2.1: Schematic illustration of clay particles and their structure. Measures are approximate. a) shows many clay particles. b) The stacking of sheets of a single clay particle. c) Zoom in on a sub-stack of clay platelets. d) Two platelets separated by a cation. e) The structure of each clay platelet. Adapted with permission from ref.[38].

To obtain electrical neutrality in the octahedral sheet different cations can occupy the octahedral sites (cation positions) of the sheet. On the basis of a half unit cell containing three octahedra there are two ways to maintain the neutrality, depending on the valency of the cation occupying the octahedral sites. If the cation has a valency of two, for example Mg^{2+} or Fe^{2+}, all three octahedral sites needs to be filled to maintain neutrality, and the clay is said to be trioctahedral. While if the valency is three, with for example Al^{3+} or Fe^{3+}, only two thirds of the sites needs to be filled to achieve neutrality, and thus the clay is dioctahedral [39, 37, 40]. Substitution for Si^{4+} in the tetrahedral sheet is also possible, but less common.

The sheets of tetrahedra (T) and octahedra (O) can be organized in two different ways [37], both displayed in fig. 2.2. The lower structure in fig. 2.2, and also displayed in fig. 2.1e), is the 2:1 structure or the T-O-T structure. In this structure one octahedral sheet is sandwiched between two tetrahedral sheet. Such a layer of connected tetrahedra and octahedra are often called platelets and are the building blocks of the clay particles. Figure 2.1a-d) shows how the repetition of the T-O-T structure, or clay platelets, stacked on top of one another creates the clay particle. In a similar manner the upper structure in fig. 2.2, called 1:1 or T-O-structure, is composed of one tetrahedral sheet connected to an octahedral sheet. This also makes up one clay platelet, and can be stacked in the same way as shown in fig. 2.1.

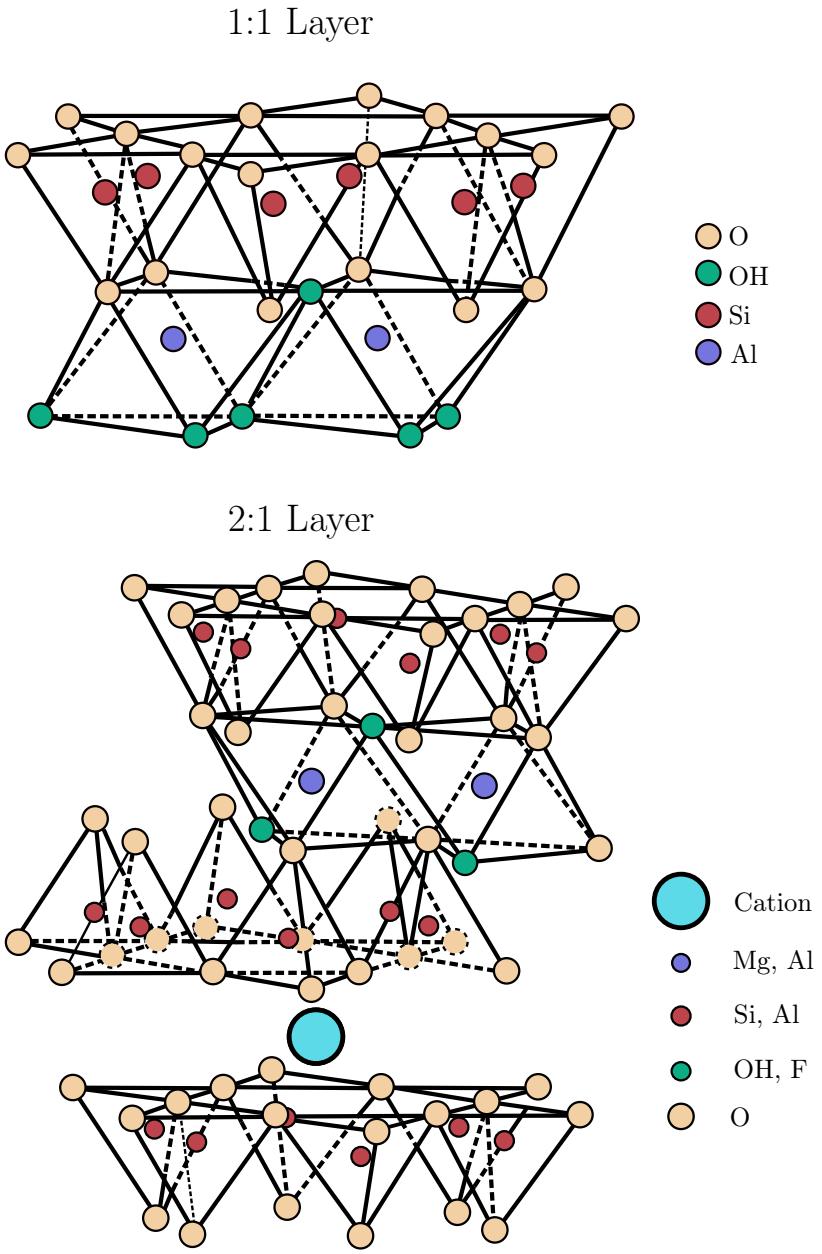

Figure 2.2: Illustrating the 1:1 and 2:1 layer structure of clay minerals. Top: 1:1 structure with one tetrahedral layer connected to an octahedral layer. Bottom: 2:1 structure where one octahedral layer is sandwiched between two tetrahedral layers. A cation (blue point) resides between one 2:1 layer and another. The purple points show the octahedral sites, the red are the tetrahedral sites, the green are the hydroxyls or fluorine groups. All other points are oxygen. Figures adapted with permission from refs.[38, 41].

2.1.2 Interlayer cation and swelling

From fig. 2.1e) it can be seen that there are spaces between each T-O-T layer, which in fig. 2.1e) is occupied by a cation. This space is often called the interlayer space and is empty for electrically neutral layers, which are held together through van der Waals interactions [37]. However, as mentioned earlier different cations can occupy the sites in the tetrahedra and octahedra, producing neutral layers. Through isomorphous substitution, meaning that an atom is exchanged for another without changing the structure of the crystal, the platelets can obtain a net negative charge. For the negatively charged platelets to stack and form a clay particle, the charge needs to be compensated. Such a compensation is achieved through intercalating cations into the space between the platelets. These cations are often called charge compensating cations, and some common cations are Na^+, Li^+ and Mg^{2+}. Depending on the size of the cation, the strength of the interaction with the clay, the solvation energy and other factors such as their ability to polarize molecules and the location of the charges, the swelling abilities of the clay particles can differ immensely [23, 25, 42, 37].

As molecules enter the interlayer space, the clay particle swells, meaning that the distance between the top and bottom of two adjacent platelets, also called interlayer distance, increases. Such an introduction of molecules into the interlayer space is often termed intercalation, and this term will be frequently used throughout this work. This swelling has two regimes called crystalline swelling and osmotic swelling [43]. In the crystalline swelling domain the lamella structure of the clay particles is still intact, and attractive forces are dominant between the platelets. Further swelling introduces the osmotic regime where the interaction become repulsive and cause exfoliation of the clay platelets. The intercalation studied in this thesis is within the crystalline swelling regime. This swelling may happen in a stepwise fashion where the interlayer is first filled up with one layer of the foreign molecule before a new layer is started. These distinct swelling steps are often called zero water layers (0WL), 1WL, 1.5WL, 2WL and 3WL, indicating the number of water layers inside the interlayer, where 0WL is the dry state. As the intercalation of CO_2 is investigated the notation of WL will rarely be used, and formulations such as zero layers of CO_2 or one CO_2 layer will be used instead.

Another interesting feature of the swelling behaviour of the clay particles is the swelling hysteresis that some clays posses. As clays are exposed to foreign molecules there usually exists a boundary, often in terms of pressure and temperature, for intercalation of the molecules. After the swelling has begun, returning to the boundary condition will not release the intercalated molecules. To do this it is necessary to bypass the swelling boundary by some amount, and it is this that is termed the swelling hysteresis or retention. This property is especially interesting when considering clay rich rocks for CO_2 storage, as the clay particles need to retain the CO_2 even if the conditions under which it is stored are changed.

2.1.3 Fluorohectorite

To study the swelling of clay minerals when exposed to CO_2, a synthetic clay under the smectite group called fluorohectorite is used in this work. This clay is a variation of the hectorite clay, which has a 2:1 structure and a general chemical formula (half unit cell) of

$$\mathrm{M}_{\frac{x}{v}}[\mathrm{Mg}_{(3-x)}\mathrm{Li}_x]\mathrm{Si}_4\mathrm{O}_{10}(\mathrm{OH})_2,$$

where M denotes the interlayer cation, v is the valence of the cation and x is the amount of Li^+ replacing the Mg^{2+} [37]. However, in the fluorohectorite the OH-groups have been replaced by fluorine, so that the chemical formula becomes [21, 44]

$$\mathrm{M}_{\frac{x}{v}}[\mathrm{Mg}_{(3-x)}\mathrm{Li}_x]\mathrm{Si}_4\mathrm{O}_{10}\mathrm{F}_2.$$

This synthetic clay has a great charge homogeneity and few impurities, making it a good model system to investigate clay crystalline swelling due to CO_2 absorption [44]. The charge per formula unit used in this work is $\frac{x}{v} = 0.5$.

2.2 X-ray diffraction

X-ray diffraction is an important technique that has been used for over 100 years to determine crystal structures [45]. This technique exploits the X-ray scattering patterns from atoms in periodic arrays, as a result of constructive and destructive interference of the X-rays, to understand the structural arrangements of the crystal lattice. In addition to determining the crystal structures, X-ray diffraction can also help to determine strain in the probed material [46], particle sizes [47], degree of orientation [48] and particle topology [43] to mention some examples. Furthermore, X-ray diffraction can be applied to a wide variety of materials such as metals, minerals and biological material [49]. Moreover, the use of X-ray diffraction is not limited to solid materials, but applicable to liquid solutions and suspensions as well.

Due to the versatility of the X-ray diffraction it has become the Swiss army knife of crystallographic science, and it is the most popular method to characterize materials [45]. For studying intercalation of CO_2 in clay minerals, X-ray diffraction is the "weapon of choice", as the intercalation induces changes in the structure of the clay particle that can be observed as changes in the X-ray diffraction pattern.

2.2.1 Bragg's law

In order to interpret the data gained through X-ray diffraction experiments, an important concept to understand is Bragg's law. Bragg's law was developed by the father and son, William and Lawrence Bragg soon after the first diffraction of X-rays was observed by Max von Laue and his coworkers [45]. The law gives the condition for constructive interference between two scattered waves, and thus explains how the constructive and destructive interference of the scattered waves create intensity peaks and troughs.

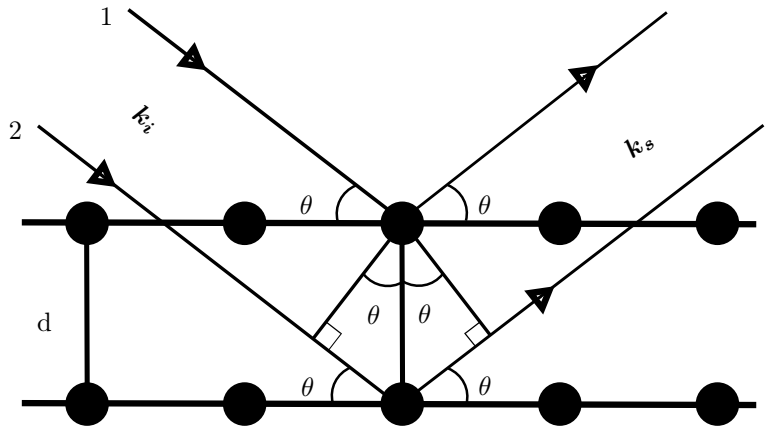

Figure 2.3: Schematics showing specular scattering of two incident rays from two parallel planes. The distance between the planes is denoted by d, and the incident and scattering angle is θ. The lines drawn normally onto the second wave from the first scatterer, marks the additional path length travelled by the second wave.

Figure 2.3 shows specular reflection of two parallel waves with the same wavelength, and is the starting point for deriving Bragg's law. For the scattered waves to interfere constructively the difference in travelled path length must equal an integer multiple of the wavelength. From the geometry of fig. 2.3 it can be seen that the

extra distance travelled by the second wave is equal to $2d\sin\theta$, where d is the distance between the planes, and θ is the incident angle. Bragg's law can thus be stated as

$$2d\sin\theta = \mathrm{n}\lambda,$$

where n is the order of diffraction, which is an integer, λ is the wavelength and θ is the angle of incidence. If Bragg's condition is fulfilled the constructive interference will result in intensity peaks at certain angles in the recorded diffractograms, which can be used to reveal the structure of the material.

2.2.2 Reciprocal space and Laue's diffraction condition

Although Bragg's law gives a basic understanding of X-ray scattering and yields good results it has some limitations. For example it does not take into account that X-rays are actually scattered from electrons in the material, rather than being reflected from planes. In addition to this, Bragg's law gives no information of the intensity of the scattered waves. Fortunately, another formulation of the diffraction condition exists, namely Laue's diffraction condition, of which Bragg's law is a special case. This diffraction condition looks at the requirements for constructive interference from two point scatterers rather than from two planes, and gives the basis for deriving a relation for the intensity. However, to be able to understand Laue's diffraction condition it is necessary to recap some important concepts from solid state physics.

Primitive translation vectors

Figure 2.4 shows a two dimensional (2D) lattice with two sets of primitive translation vectors, $\boldsymbol{a_1}$ and $\boldsymbol{a_2}$, shown in red and green. Using primitive translation vectors, it is possible to create a vector that translates from one point in the lattice to any other point in the lattice, thus describing the whole lattice. Such a vector can be written as $\boldsymbol{R} = \boldsymbol{r} + u\boldsymbol{a_1} + v\boldsymbol{a_2}$, where $\boldsymbol{r}$ is a lattice point, and u and v are integers. This can easily be expanded to 3D with a third primitive translation vector, $\boldsymbol{a_3}$, and an integer w yielding $\boldsymbol{R} = \boldsymbol{r} + u\boldsymbol{a_1} + v\boldsymbol{a_2} + w\boldsymbol{a_3}$.

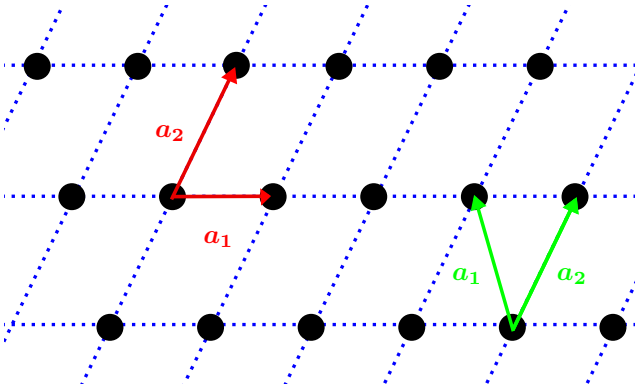

Figure 2.4: A 2D lattice with two pairs of primitive translation vectors $\boldsymbol{a_1}$ and $\boldsymbol{a_2}$ connecting the lattice points.

Miller indices

Another important tool in crystallography is the Miller indices. These indices points to specific planes in a crystal structure, and are denoted by (hkl), where h, k, l are integers. The hkl indices of a plane are found through determining the points of intersection between the plane and the axes along the three primitive translation vectors $\boldsymbol{a_1}$, $\boldsymbol{a_2}$ and $\boldsymbol{a_3}$, taking the reciprocal of them and reducing these to the smallest integers having the same ratio [50]. For planes parallel to some of the axes, the value of intersection is infinity, and the reciprocal thus becomes zero. An example to visualize this is to look at the cubic crystal in fig. 2.5. The plane indicated in fig. 2.5 intersects the a_1 axis at 1, the a_2 axis at 1, but is parallel to the a_3 axis. The reciprocal of these numbers are 1, 1 and 0, and the Miller indices of this plane is thus (110).

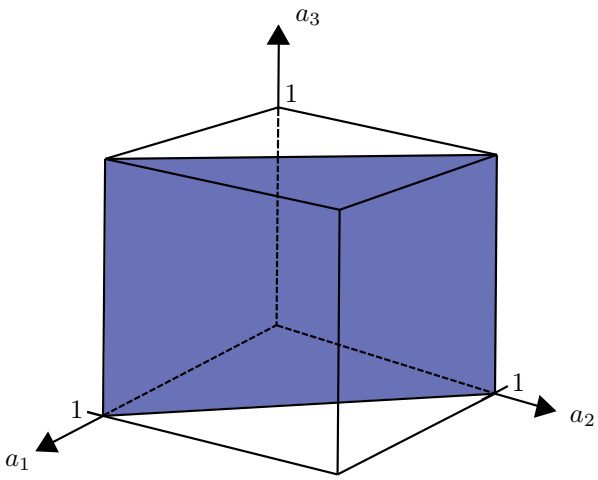

Figure 2.5: Cubic crystal with the (110) plane indicated by the shaded area.

Reciprocal space

As mentioned previously, X-ray diffraction is a tool to unravel the crystal structure of a material. In contrast to a light microscope, where the image is a magnification of the real structures, X-ray diffraction provides a more indirect image of the real structure. As only the scattered waves that constructively interfere are detected, the atoms themselves cannot be observed, and the diffraction pattern is a depiction what is called the reciprocal lattice of the structure [50]. Thus, in order to analyze the diffraction pattern a relationship between the reciprocal space and real space is needed. This is achieved though defining three primitive vectors of the reciprocal lattice $\boldsymbol{b_1}$, $\boldsymbol{b_2}$ and $\boldsymbol{b_3}$ such that:

$$\boldsymbol{b_1} = 2\pi \frac{\boldsymbol{a_2} \times \boldsymbol{a_3}}{\boldsymbol{a_1} \cdot \boldsymbol{a_2} \times \boldsymbol{a_3}}, \quad \boldsymbol{b_2} = 2\pi \frac{\boldsymbol{a_3} \times \boldsymbol{a_1}}{\boldsymbol{a_1} \cdot \boldsymbol{a_2} \times \boldsymbol{a_3}}, \quad \boldsymbol{b_3} = 2\pi \frac{\boldsymbol{a_1} \times \boldsymbol{a_2}}{\boldsymbol{a_1} \cdot \boldsymbol{a_2} \times \boldsymbol{a_3}}.$$

These vectors are the primitive vectors for the reciprocal lattice, and with these it is possible to construct a reciprocal lattice vector in a similar manner as for real space. A reciprocal lattice vector would thus be represented by $\boldsymbol{G}_{hkl} = h\boldsymbol{b_1} + k\boldsymbol{b_2} + l\boldsymbol{b_3}$, where h, k, l are integers. From the definition of the primitive reciprocal lattice vectors it can also be seen that they are defined by an area divided by a volume, making the units of the vectors inverse length.

Laue's diffraction condition

Having recapped some important tools it is now possible to derive Laue's diffraction condition. The following derivation is based on similar derivations in ref.[50] and ref.[51]. Considering elastic scattering from two point scatterers in real space, shown in fig. 2.6.

Two incoming waves have the same direction and magnitude and are described by their wave vectors $\boldsymbol{k_i}$. The scattered waves in the direction of $\boldsymbol{k_s}$ have the same magnitude as the incoming waves $\boldsymbol{k_i}$, $|\boldsymbol{k_i}| = |\boldsymbol{k_s}| = k = \frac{2\pi}{\lambda}$, where λ is the wavelength. The vector between the two point scatterers is the lattice vector $\boldsymbol{R} = u\boldsymbol{a_1} + v\boldsymbol{a_2} + w\boldsymbol{a_3}$. Now, as for Bragg's law, it is necessary to find the path difference between the two incoming waves, which should equal an integer number of the wavelength for constructive interference to occur. From the geometry in fig. 2.6, it can be seen that the path difference

$$\Delta s = \Delta s_1 + \Delta s_2.$$

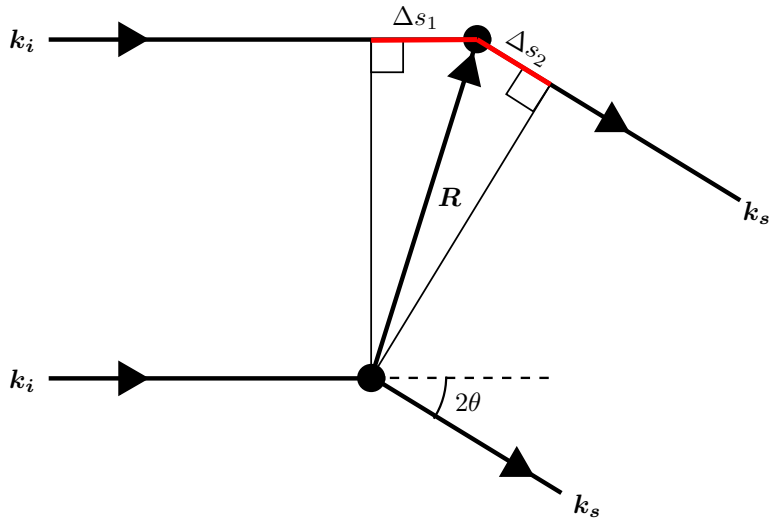

Figure 2.6: Scattering from two point scatterers with incoming waves of wave vectors $\boldsymbol{k_i}$, and scattered waves with wave vectors $\boldsymbol{k_s}$. The extra path length travelled by the second wave is shown by the red lines, constructed by the lines from the first scattering point normal on to the second wave.

Δs_1 and Δs_2 can be viewed as a projection of $\boldsymbol{R}$ along the $\boldsymbol{k_i}$ and $-\boldsymbol{k_s}$ producing the expressions

$$\Delta s_1 = \frac{\boldsymbol{R}\cdot\boldsymbol{k_i}}{|\boldsymbol{k_i}|} = \frac{\boldsymbol{R}\cdot\boldsymbol{k_i}}{k} \quad \text{and} \quad \Delta s_2 = -\frac{\boldsymbol{R}\cdot\boldsymbol{k_s}}{|\boldsymbol{k_s}|} = -\frac{\boldsymbol{R}\cdot\boldsymbol{k_s}}{k}.$$

The path difference is then given by

$$\Delta s = \frac{\boldsymbol{R}\cdot\boldsymbol{k_i}}{k} - \frac{\boldsymbol{R}\cdot\boldsymbol{k_s}}{k} = -\frac{1}{k}(\boldsymbol{k_s}-\boldsymbol{k_i})\boldsymbol{R}.$$

Defining a scattering vector $\boldsymbol{q} = \boldsymbol{k_s} - \boldsymbol{k_i}$, that has a magnitude of $q = \frac{4\pi}{\lambda}\sin\theta$ if the angle between $\boldsymbol{k_i}$ and $\boldsymbol{k_s}$ is 2θ, the condition for diffraction becomes

$$-\frac{1}{k}\boldsymbol{q}\boldsymbol{R} = \mathrm{n}\lambda.$$

When this condition is fulfilled scattering in the direction of $\boldsymbol{k_s}$ can be detected. To determine when the condition is fulfilled it is necessary to look at the vector $\boldsymbol{q}$. Using that $k = \frac{2\pi}{\lambda}$, the scattering condition reduces to

$$-\boldsymbol{q}\cdot\boldsymbol{R} = 2\pi\mathrm{n}.$$

Since $\boldsymbol{q} = \boldsymbol{k_s} - \boldsymbol{k_i}$, where both $\boldsymbol{k_i}$ and $\boldsymbol{k_s}$ are vectors in reciprocal space, $\boldsymbol{q}$ is also a vector in reciprocal space. It can thus be written as $\boldsymbol{q} = h\boldsymbol{b_1} + k\boldsymbol{b_2} + l\boldsymbol{b_3}$, where $\boldsymbol{b_1}$, $\boldsymbol{b_2}$ and $\boldsymbol{b_3}$ are the primitive vectors of the reciprocal lattice and h, k, l can be any number. Now using $\boldsymbol{R} = u\boldsymbol{a_1} + v\boldsymbol{a_2} + w\boldsymbol{a_3}$ the scattering condition becomes

$$-(h\boldsymbol{b_1} + k\boldsymbol{b_2} + l\boldsymbol{b_3}) \cdot (u\boldsymbol{a_1} + v\boldsymbol{a_2} + w\boldsymbol{a_3}) = 2\pi\mathrm{n},$$
$$(hu + kv + lw) = \mathrm{n}.$$

As u, v, w and n are integers the only way for this to be fulfilled for any $\boldsymbol{R}$ is for h, k, l to be integers. Thus for the scattering condition to be fulfilled the scattering vector $\boldsymbol{q}$ needs to be equal to the reciprocal lattice vector, $\boldsymbol{G}$. This can be written as

$$\boldsymbol{q} = \boldsymbol{k_s} - \boldsymbol{k_i} = \boldsymbol{G},$$

and is called the Laue diffraction condition.

2.2.3 Ewald sphere

The Laue diffraction condition is somewhat abstract at first glance, but using a construction called the Ewald sphere it is possible to visualize the diffraction condition. The Ewald sphere is constructed through three steps [52]:

1. Draw the reciprocal lattice.
2. Draw the vector $\boldsymbol{k_i}$ ending at a reciprocal lattice point.
3. Draw a circle with radius $|\boldsymbol{k_i}|$ around the starting point of $\boldsymbol{k_i}$.

Figure 2.7 shows the construction for a lattice in 2D. Here it can be seen that the diffraction condition $\boldsymbol{k_s} - \boldsymbol{k_i} = \boldsymbol{G}$ is only fulfilled when the circle intersects a reciprocal lattice point. This demonstrates how strict the diffraction condition is, and indicates a possible issue with low scattering intensity. It should also be noted that the radius of the sphere is dependent on the wavelength, being $R = |\boldsymbol{k_i}| = \frac{2\pi}{\lambda}$.

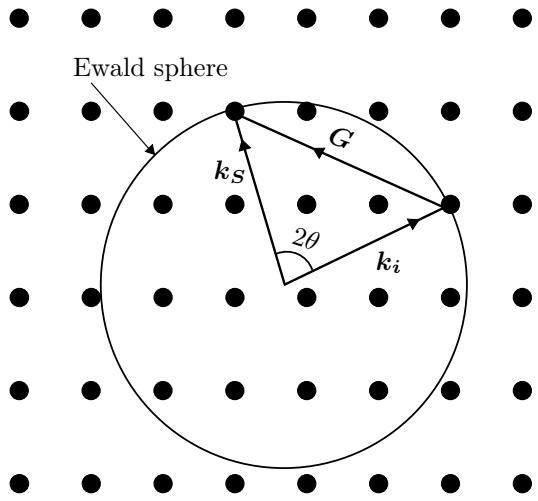

Figure 2.7: The Ewald sphere construction. $\boldsymbol{k_i}$ and $\boldsymbol{k_s}$ are the incident and scattered wave vectors, with a scattering angle of 2θ. The difference between $\boldsymbol{k_i}$ and $\boldsymbol{k_i}$ is the scattering vector $\boldsymbol{q}$, stretching between two lattice points. Where the circle of radius k intersects a lattice point there will be scattering in that direction.

A neat solution to obtain additional scattered waves is to use powders. In a powder there will be crystals of every possible orientation. Different orientations of the crystal corresponds to rotating the reciprocal space and thus there will always be some crystals that fulfill the diffraction condition. In fig. 2.8 each circle now corresponds to a point that has been rotated 360° around the origin of the reciprocal lattice, chosen to be the atom at the end of $\boldsymbol{k_i}$. Each circle (except the Ewald sphere) in fig. 2.8 represents the rotation of the intersecting atoms about the origin, and thus each point on the circle is a reciprocal lattice point. When drawing the Ewald sphere (red circle) it can be seen by symmetry that for each other circle it intersects there are two points of intersection, giving two directions where scattering can be detected. These examples have demonstrated the Ewald construction in 2D, however it can be expanded to 3D. The Ewald construction then becomes a sphere, and the same is the case for the circles drawn for the lattice point now rotated around a third axis. This produces an intersection of two spheres for powders, and the diffraction pattern of a powder recorded with an area detector is thereby made up of rings, which are often called Debye-Scherrer rings.

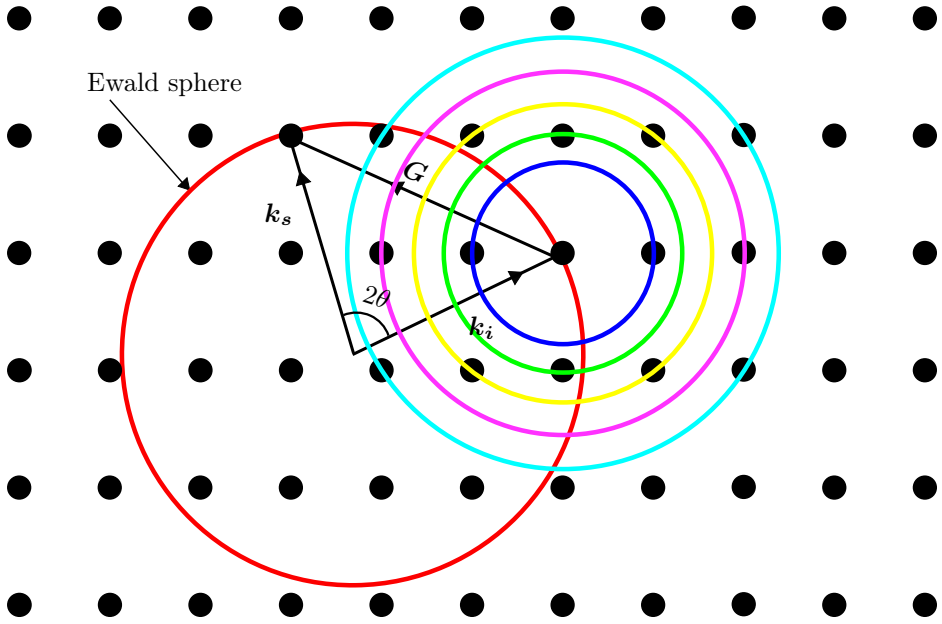

Figure 2.8: Ewald construction in powder. The Ewald circle is drawn in red, while the other circles represent a lattice point that has been rotated, covering all orientations of grains in the powder. Where the Ewald circle intersects one of the other circles there will be scattering in that direction.

2.2.4 Relating the *hkl* plane to the reciprocal lattice vector

As mentioned earlier each of the points in the diffraction image are related to the reciprocal lattice of the structure that scattered the X-rays. The reciprocal lattice is related to the real structure through the vectors $\boldsymbol{b_1}$, $\boldsymbol{b_2}$ and $\boldsymbol{b_3}$, but this does not explain what the reciprocal lattice points represent. To show this, assume that the vector $\boldsymbol{G_{hkl}}$ is perpendicular to a plane in real space. Then the cross product between the reciprocal lattice vector and the normal vector of the plane must equal zero.

Figure 2.9 shows a plane intersecting the axes in the direction of the primitive translation vectors $\boldsymbol{a_1}$, $\boldsymbol{a_2}$ and $\boldsymbol{a_3}$. The intercepts are expressed in terms of these vectors and can be written as $u\boldsymbol{a_1}$, $v\boldsymbol{a_2}$ and $w\boldsymbol{a_3}$. Denoting

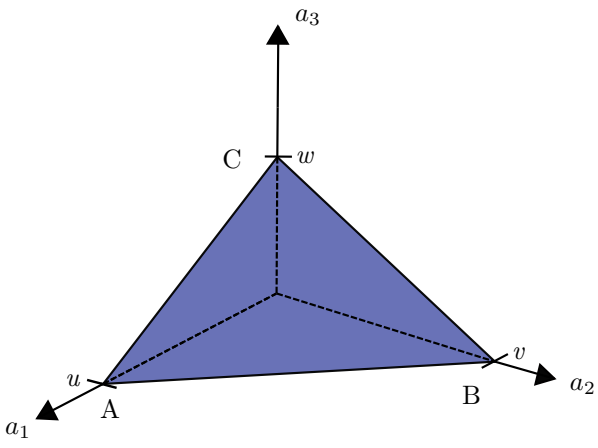

Figure 2.9: Crystal with axes $\boldsymbol{a_1}$, $\boldsymbol{a_2}$, $\boldsymbol{a_3}$, and a plane (shaded in blue) intersecting the axes at the points ua_1, va_2 and wa_3.

the points of intersection as A, B and C, a normal vector, $\boldsymbol{N}$ of the plane can be constructed through a cross product of $\boldsymbol{AB}$ and $\boldsymbol{AC}$. This yields the normal vector

$$\boldsymbol{N} = -uw\boldsymbol{a_1} \times \boldsymbol{a_3} - uv\boldsymbol{a_2} \times \boldsymbol{a_1} + vw\boldsymbol{a_2} \times \boldsymbol{a_3}.$$

Using the definitions of $\boldsymbol{b_1}$, $\boldsymbol{b_2}$ and $\boldsymbol{b_3}$ this can be rewritten as

$$\boldsymbol{N} = \frac{V}{2\pi}(vw\boldsymbol{b_1} + uw\boldsymbol{b_2} + uv\boldsymbol{b_3}),$$

where $V = \boldsymbol{a_1} \cdot \boldsymbol{a_2} \times \boldsymbol{a_3}$.

The normal vector is thus a vector in reciprocal space. Crossing the normal vector with $\boldsymbol{G_{hkl}}$ produces three equations for the product to equal zero.

$$\frac{k}{l} = \frac{w}{v}, \qquad \frac{h}{l} = \frac{w}{u}, \qquad \frac{h}{k} = \frac{v}{u}.$$

The miller indices are found through taking the reciprocal of the intercepts of the plane, and thus the miller indices for the plane become $(\frac{1}{u}\frac{1}{v}\frac{1}{w})$. Exchanging the intercepts with the miller indices in the equation above it turns out that $u : v : w$ must equal $h : k : l$ for the plane of Miller indices $(\frac{1}{u}\frac{1}{v}\frac{1}{w})$ to be perpendicular to $\boldsymbol{G_{hkl}}$. Thus the Miller indices multiplied by a constant have to equal h, k, l, and each point on the diffraction image represents a plane of miller indices (hkl) or a multiple thereof.

2.2.5 Contributions to the diffracted intensity

Bragg's law gives useful insight, but yields no way of calculating the intensity of the diffraction. This was the motivation for deriving Laue's diffraction condition. Using the concepts developed through the derivation of the Laue condition it is now possible to write an expression for the intensity. To have diffraction at all, the diffraction condition needs to be fulfilled, however there are several parameters that affect the resultant measured intensity.

Electrons in crystals scatter X-rays by interacting with the electric field of the wave. This causes the electrons to start oscillating at the same frequency as the electric field and radiate X-rays is a all directions. For a single free electron interacting with X-rays, the intensity of the scattered wave will be $I \propto |E_0|^2$ [52].

Scattering from individual electrons around an atom will give rise to constructive and destructive interference of the scattered waves. Due to this, the resultant amplitude will decrease with increasing scattering angle, reducing the overall intensity. This can be described through the scattering power of an atom, and is done through a parameter called *atomic form factor* [50],

$$f_j(\boldsymbol{q}) = \int n_j(\boldsymbol{r}) \mathrm{e}^{-i\boldsymbol{qr}} dV.$$

Here $\boldsymbol{q}$ is the scattering vector introduced in section 2.2.2, j denotes the atom, $n_j(\boldsymbol{r})$ is the electron concentration at a position $\boldsymbol{r}$ due to the contribution from atom j, and $\mathrm{e}^{-i\boldsymbol{qr}}$ is a phase term that modulates the scattering power for different angles of diffraction. If $\boldsymbol{q} \to 0$ the integral equal to the number of electrons of atom j, Z, and the scattering is maximal in the forward direction [53].

Having the scattering power of each atom it is possible to consider an ensemble of atoms collected in a molecule. The scattering from such a unit will then comprise a sum of all the form factors of the different atoms multiplied by another phase term, and is called *molecular structure factor* [53]:

$$F^{mol}(\boldsymbol{q}) = \sum_{\boldsymbol{r}_j} f_j(\boldsymbol{q}) \mathrm{e}^{-i\boldsymbol{qr_j}}.$$

This molecular structure factor can now be utilized to find a similar expression for the whole crystal structure. Crystals are composed of a repeating unit, called the unit cell. This unit cell can have a basis of one atom, or of molecules making the final crystal structure. Thus, to find an expression for the scattering from the crystal lattice it is necessary to sum up the contributions from the unit cells and add a phase term for the lattice. The structure factor for a crystal then becomes

$$F^{crystal}(\boldsymbol{q}) = \underbrace{\sum_{\boldsymbol{r}_j} F^{mol}(\boldsymbol{q}) \mathrm{e}^{-i\boldsymbol{qr_j}}}_{\text{Unit cell structure factor}} \underbrace{\sum_{\boldsymbol{R}} \mathrm{e}^{-i\boldsymbol{qR}}}_{\text{Lattice sum}},$$

where $\boldsymbol{R} = u\boldsymbol{a_1} + v\boldsymbol{a_2} + w\boldsymbol{a_3}$, is the origin of the unit cell [53]. Now, the structure factor will be non-zero when the scattering condition $\boldsymbol{q} = \boldsymbol{G}$ is fulfilled, and the intensity is then related to the structure factor through $I \propto I_0 F^{crystal}(\boldsymbol{q}) \cdot F^{crystal}(\boldsymbol{q})^* = I_0 |F^{crystal}|^2$ where I_0 is the incoming intensity. Thus, depending on the position of the atoms, scattering from certain planes may be extinguished through destructive interference, while others are clearly visible and the intensity is governed by the structure factor.

On the other hand, the intensity is not solely determined by the structure of the material. External factors, such as the Debye-Waller factor, the Lorentz factor, and the polarization factors also modifies the scattered intensity and will be briefly discussed.

The Debye-Waller factor is a correction on the atomic form factor due to vibrations of the atoms in the lattice. These vibrations give rise to an attenuation of the scattered intensity, and can be accounted for by changing the phase factor of the form factor to be $\mathrm{e}^{-\frac{1}{2}q^2\langle u_q^2\rangle} = \mathrm{e}^{-M}$, where $\langle u_q^2 \rangle$ is a time average of the square displacement of the atoms. The resulting form factor thus becomes

$$f_j(\boldsymbol{q}) = \int n_j(\boldsymbol{r}) \mathrm{e}^{-M} dV.$$

For more detailed description of the Debye-Waller factor and its implications see ref.[53].

In addition to the Debye-Waller factor there is also the Lorentz-polarization factor which is combined of the polarization factor P, and the Lorentz factor L. The polarization factor P comes from the fact that the observed intensity is dependent on the polarization of the incident X-rays and the angle and plane the scattering is observed in. This can be written as

$$P = \begin{cases} 1 & \text{synchrotron: vertical scattering plane} \\ \cos^2\phi & \text{synchrotron: horizontal scattering plane} \\ \frac{1}{2}(1+\cos^2\phi) & \text{unpolarized source,} \end{cases}$$

where ϕ is the angle of observation [53]. The result of the polarization factor is to decrease the observed intensity.

The Lorentz factor, which accounts for the fact that there might be diffraction at angles that differ slightly from the Bragg angle. It also takes into account the amount of grains favorably oriented for diffraction at a certain angle. Together with the polarization factor the Lorentz-polarization factor may be written [19]

$$L_p = \frac{2P}{\sin 2\theta \sin^v \theta},$$

where v is the factor accounting for the number of grains favorably oriented and θ is the scattering angle. v takes on a value between 0 and 1, where 0 is for a perfect crystal, and 1 is for a perfect powder [19].

There are other factors that also contribute to the intensity, such as multiplicity and absorption [53]. Multiplicity arises from the number of equivalent planes in the crystal, all contributing to the scattering at the same angle, thereby increasing the scattered intensity. Absorption on the other hand attenuates the X-rays and is dependent on the amount of material in the sample and its interaction with the X-rays.

Excluding the multiplicity and absoprtion contributions to the intensity a final relation for the intensity can be constructed by the Lorentz-polarization factor and the structure factor, and becomes

$$I \propto I_0 |F^{crystal}|^2 L_p.$$

An important thing to note is that through diffraction experiments the phase information is lost, and thus it is not possible to directly calculate the structure of the material. To find the structure, the collected data needs to be compared to theoretically modeled structures and refined until a good match is found. The loss of the phase is often called *the phase problem* and makes the process of determining the structure of the material more cumbersome.

3 Experimental section

To study the interactions of clay minerals and CO_2, experiments have been performed at two different synchrotron radiation facilities. The two facilities used were the European Synchrotron Radiation Facility (ESRF) in France and the Laboratório Nacional de Luz Síncrotron (LNLS) in Brazil. Both the ESRF and LNLS provide X-rays of high energy suitable for X-ray diffraction. This yields high quality diffraction images, with the source at ESRF being a third generation synchrotron and the one at LNLS being a second generation source. In this section the structure and working principle of a synchrotron will be explained, as well as a description of the equipment and setup used for each experiment. The sample preparation will also be presented.

3.1 Synchrotron radiation

The principle of a synchrotron X-ray source is that electrons being accelerated create intense X-ray radiation that can be exploited for scientific purposes. A synchrotron light source is composed of several units; an electron source, a linear accelerator, a booster ring, a storage ring and the beamlines. The following description of a synchrotron is based material from ref.[54].

In a linear accelerator electrons are produced by an electron gun and accelerated to high energies before being injected into the booster synchrotron. The electron gun producing the electrons consists of a cathode, an anode and a voltage supplied between the anode and cathode. When the cathode is heated, the electrons in the material of the cathode gain enough energy to be released from the surface. The potential difference between the cathode and anode will then accelerate the electrons towards the anode. After the electrons pass through the anode they are accelerated in the linear accelerator by radio-frequency (RF) cavities to sufficiently high energies for injection into the booster synchrotron.

The booster synchrotron ring is where the electrons are further accelerated by RF cavities before injection into the storage ring. To keep the electrons circulating until desired energy is reached, strong magnets are used to bend the electrons. The magnetic fields of these magnets need to be regulated during the acceleration of the electrons to prevent loss of electrons. After the electrons have reached the desired energy they are injected into the larger storage ring where the X-ray production occurs. Depending on the type of synchrotron, different schemes for refilling the storage ring are used, and the two synchrotrons used for the experiments in this thesis are examples of this. The ESRF runs a mode called top-up mode [55]. This means that every 20 min the storage ring is refilled, and thus the linear accelerator and booster synchrotron are in use quite frequently. In contrast to this, LNLS operates in decay mode, where there is only two refills of the storage ring during 24 h [56]. The two different types of refilling the storage ring affects the beam current quite dramatically. For the top-up model the beam current is close to constant, whereas for the LNLS the beam current decreases exponentially from one injection to the next.

The storage ring is a set of straight and curved segments lined with different types of magnets. In the curved sections there are bending magnets, bending the electrons in a curve. Here the electrons will produce a splay of X-rays as they are bent, and in the second generation synchrotrons this is the radiation that is used for experiments. After the bending magnets there are focusing magnets in the straight section, ensuring that the electrons keep an ideal path through the ring. For third generation synchrotrons the straight sections are also equipped with insertion devices, such as wigglers or undulators. These are arrays of closely spaced magnets bending the electrons in a wavy path creating a highly focused and intense beam of X-rays that can be used in the beamlines. As the electrons radiate away energy in form of X-rays, this energy needs to be replenished. In the top-up mode this is done both by refilling the ring with electrons frequently and by RF cavities, while for the LNLS new energy is provided by RF cavities placed in the storage ring, enabling stable operation.

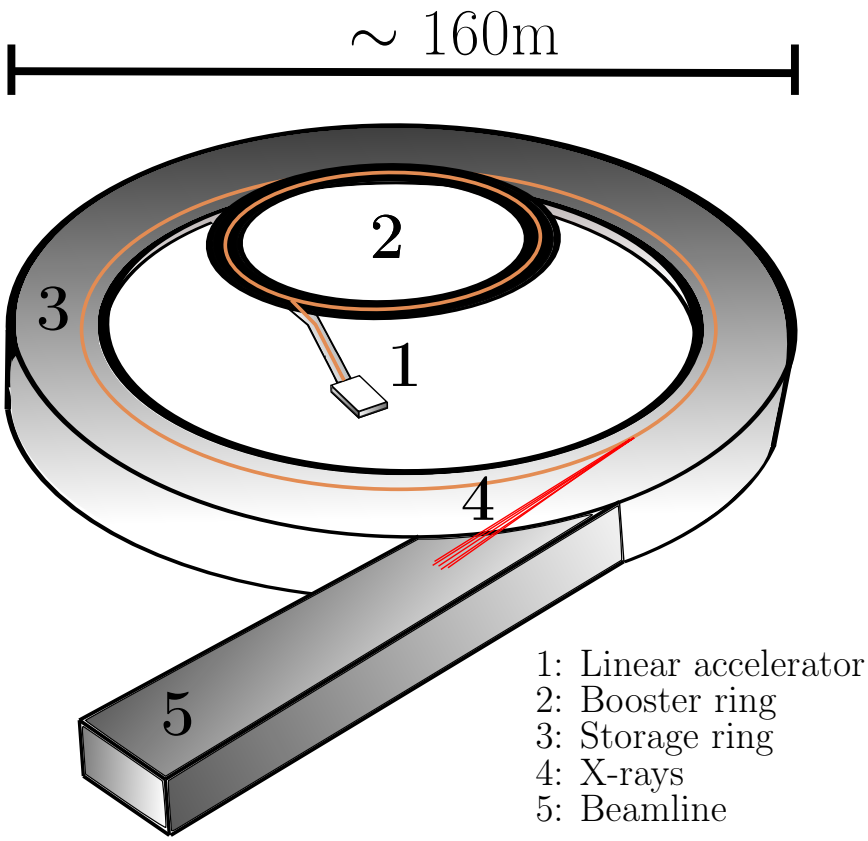

Figure 3.1: The general setup of a synchrotron radiation facility. The linear accelerator (1) is in the middle of the synchrotron, supplying the smaller booster ring (2) with electrons, before they are injected into the storage ring (3) and subsequently emit X-rays (4) supplied to the beamlines (5).

When X-rays are produced, they are directed toward beamlines where experiments are conducted. However, before the X-rays can be used in experiments it is necessary to perform some manipulation of the beam to suit the purpose of the experiments. This is achieved through X-ray optics using mirrors, monochromators, pinholes and slits to modify the beam energy and size. After the user specific changes have been applied, the beam arrives at the sample in the experimental hutch and data can be collected.

3.2 Experimental setup at ESRF

Beam and detector specifications
At the Swiss-Norwegian beamline, BM01, at ESRF a monochromatic beam of wavelength $\lambda = 0.775\,\text{Å}$ and area $0.2\,\text{mm} \times 0.2\,\text{mm}$ was used. A Si(111) double-crystal was utilized to make the beam monochromatic and focus it towards the sample through the slits. The scattered intensity was recorded using a Pilatus 2M area detector, at a distance of 439 mm from the sample. A protective sheet of Kapton was placed in front of the detector. A LaB_6 sample was used as the calibrant. The setup can be seen in fig. 3.2. The technical information of the experiment is summarized in table 1.

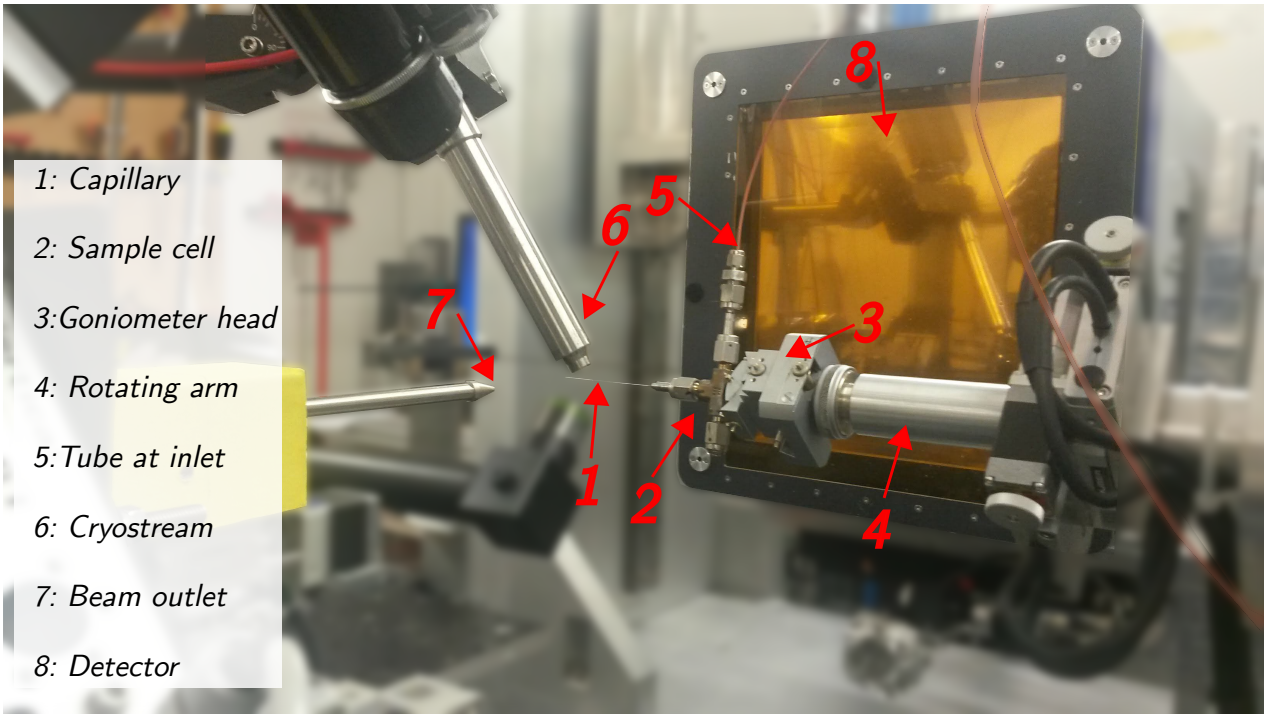

Figure 3.2: The setup used at ESRF. The capillary (1) was mounted in the sample cell (2). The sample cell and goniometer head (3) were attached to a rotating arm (4). A tube for CO_2 (5) was mounted on the sample cell. Above the capillary a cryostream (6) was mounted to control temperature. The beam exited from the thin arrow-shaped pipe (7) pointing at the capillary. The detector (8) was placed behind the capillary, and is visible behind the yellow sheet of Kapton.

Table 1: The technical information of the experiment performed at ESRF.

Technical specifications	
Wavelength	0.775 Å
Monochromator	Si(111) double-crystal
Beam area	0.2 mm × 0.2 mm
Detector	Pilatus 2M
Sample-to-detector distance	439 mm
Calibrant	LaB_6

Sample cell

The sample cell is described in ref.[57] as sample cell B, and is designed to investigate solid-gas interactions by *in-situ* powder X-ray diffraction. From fig. 3.3 it can be seen that the sample cell consists of a Tee-connection (4) with two inlets (5,6). The inlets lead to the sample residing in a capillary (1) mounted on the cell. To mount the capillary on the sample cell a weld gland (2), a gasket and a female nut (3) was used. The capillary filled with sample was inserted into the weld gland with the funnel at the broader end of the weld gland. It was then glued to keep the pressure and prevent the capillary from being blown out of the weld gland as pressure was applied. After the glue had dried, the funnel was broken and the gland plus capillary was inserted into a female nut before placing a gasket on top of the weld gland and screwing it to the sample cell. The sample cell was placed on a goniometer head mounted on a motor that rotated the sample ±180° during the measurements. The goniometer head was used to align the sample. This was necessary to avoid that the capillary moved in and out of the beam, and assure that the beam hit the center of the capillary as it rotated.

In the experiments only one of the inlets were used for injection of CO_2 and pumping vacuum on the sample. The other inlet was closed so that no air (including O_2, N_2, water vapor etc.) could enter the sample cell.

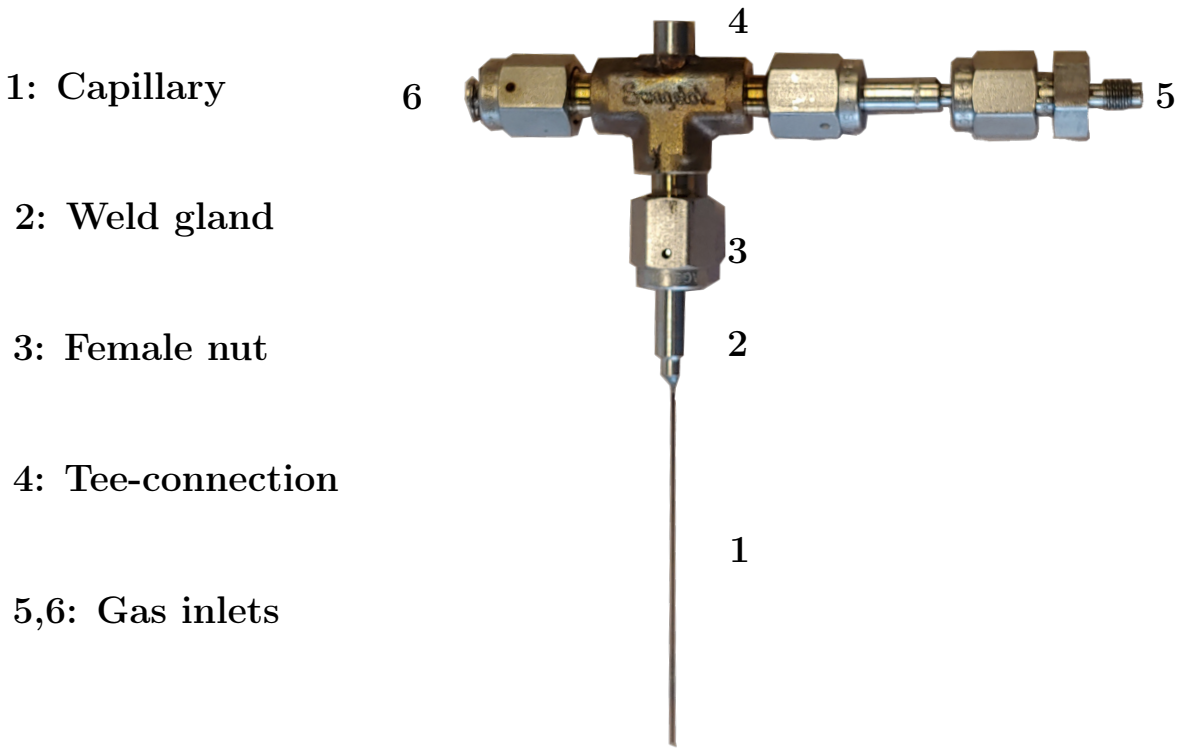

Figure 3.3: Image of the high pressure sample cell used in the experiments. The capillary (1) was connected to the Tee-connection (4) of the cell with a weld gland (2) and a female nut (3). The two inlets can be used to expose the sample to different gases. For the CO_2 exposure, the inlet numbered 5 was used, while the other inlet (6) was sealed. Image credit: Kristoffer W.B. Hunvik

Pressure and temperature control
To control the CO_2 pressure into the sample and evacuate the sample, a valve system connected to the sample cell on one side, and to both a bottle of CO_2 and a turbo pump on the other side, was used. The purity of the CO_2 utilized in the experiment was 99.9995 %, and the turbomolecular pump was of the type Pfeiffer Vacuum HiCube running at a frequency of 1500 Hz.

The temperature in the sample was controlled by using an Oxford Cryostream700+ that operates from 80 K to 400 K, using a nitrogen flow directed towards the capillary to heat and cool the sample.

Sample preparation
Glass capillaries from Hilgenberg [58] of size 0.5 mm (prod.nr 4007605) and 0.3 mm (prod.nr 4007603) and a wall thickness of 0.01 mm were loaded with Nickel fluorohectorite powder synthesized by Prof. Josef Breu's group at The University of Bayreuth [44]. A bundle of glass wool was then inserted into the capillary near the funnel. The purpose of the glass wool was to prevent the clay from escaping the capillary as vacuum was pumped. Lastly the sample was glued with epoxy to a weld gland and placed in the sample cell as described above.

3.3 Experimental setup at LNLS

Beam and detector specifications
The measurements at the beamline XRD2 at LNLS were performed using a parallel beam of wavelength $\lambda = 1.305\,\text{Å}$ and area $0.3\,\text{mm}\times0.3\,\text{mm}$, monochromatized by a Si(111) double-crystal. A Pilatus 300K area detector was used to record the scattered intensity, and this was placed at a distance of 114.8 mm from the sample. The sample holder with capillary was mounted on a rotating motor, however the rotation was not used in fear of destroying the motor. For protection of the detector from exploding capillaries, a sheet of Kapton was placed in front of it. The technical information is summarized in table 2.

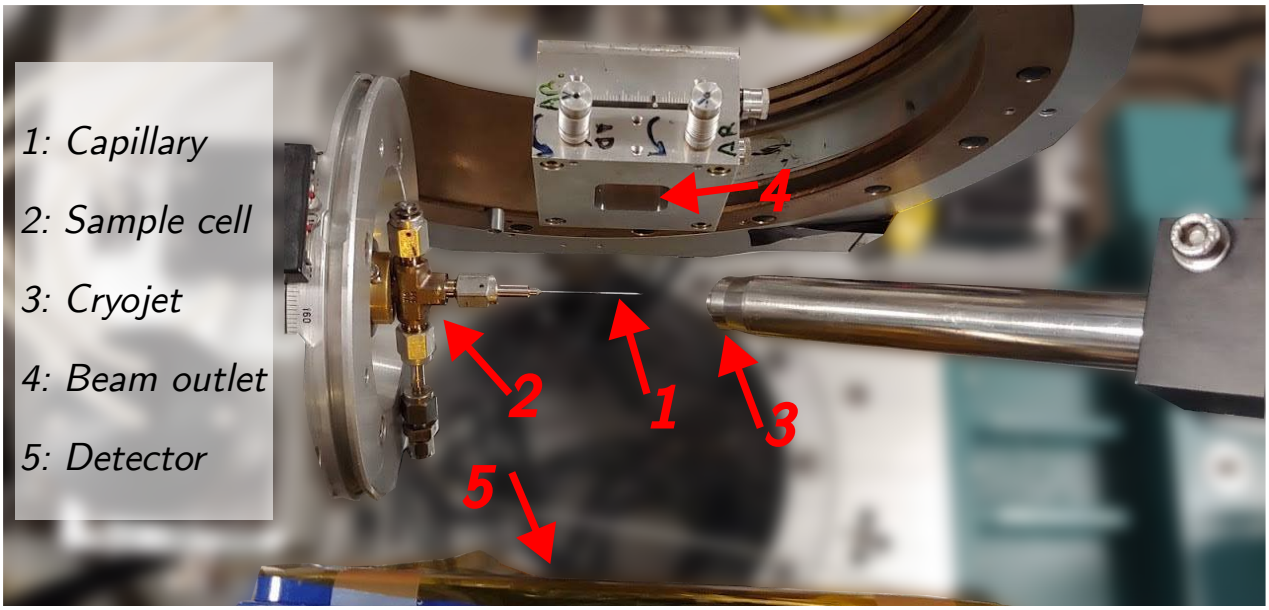

Figure 3.4: The setup used at LNLS. The capillary (1) connected to the sample cell (2) in the center of the image. The cryojet (3) is pointing towards the capillary. The beam exits from the small square metal box (4). The Pilatus detector (5) is placed close to the sample with a protective sheet of Kapton (yellow sheet). Image credit: Kristoffer W.B. Hunvik

Table 2: Table showing the technical information of the experiment performed at LNLS.

Technical specifications	
Wavelength	1.305 Å
Monochromator	Si(111) double-crystal
Beam area	0.3 mm × 0.3 mm
Detector	Pilatus 300K
Sample-to-detector distance	115 mm
Calibrant	LaB_6

Sample cell
The same custom sample cell as described for the experimental setup at the ESRF was also used at LNLS. See section 3.2 for an review of the cell.

Pressure and temperature control
The pressure and temperature control at the LNLS was similar to that used at the ESRF. For controlling the pressure a valve system connected to the sample cell, a turbomolecular pump and a bottle of CO_2 was used. The turbomolecular pump was of the same type as for the experiments at the ESRF, namely a Pfeiffer vacuum HiCube running at a frequency of 1500 Hz. As CO_2 was applied, the pressure was manually monitored by reading the pressure gauge on the valve system. The CO_2 had a purity of 99.9 %.

In order to control the temperature, the Oxford Cryojet5 was used. This has a temperature range of 85 K to 500 K, and operates by using a nitrogen flow directed towards the capillary. To monitor the temperature close to the capillary, an additional thermocouple was used. This was manually checked to ensure that the temperature set by the cryojet was similar to the one measured near the capillary.

Sample preparation
The different clay powders [44] were loaded into separate Hilgenberg glass capillaries [58] of size 0.5 mm (prod.nr 4007605) with a wall thickness of 0.01 mm. Glass wool was inserted before gluing the capillary with epoxy to the weld gland, breaking the funnel and mounting it on the sample cell.

4 Data acquisition and handling

To obtain data of good quality, revealing the specific information wanted, some preparation and subsequent data handling is necessary. The preparations included a consideration of what information was desired, and which instrumentation and setup would enable the collection of said data. Examples of such parameters are choice of wavelength and choice of scattering range/sample-to-detector distance.

4.1 Calibration

The 2D diffraction patterns of powders acquired by an area detector display rings of different radii, centered at the direct beam. An example of this can be seen in fig. 4.1(a), showing a diffraction pattern of Nickel-fluorohectorite. The radius, or position of the rings can be related to the scattering angle of the detected wave. However, to get the correct scattering angle the distance from the sample to the detector has to be accurately determined. This is done through measuring a calibration sample. Two common calibration samples are Silver-Behenate (AgBh) and Lanthanum hexaboride (LaB_6). Both of these samples have a known structure and an X-ray diffraction pattern of multiple, sharp rings. Since the structure is known, the correct positions/angles of the diffraction rings are also known, making it possible to calculate the sample-to-detector distance by comparing the measured positions with the theoretical ones. A crucial parameter for this calibration is the position of the direct beam, which is needed to correctly determine the position of the diffraction rings. To determine the beam center, a measurement of an attenuated direct beam can be performed.

4.2 Corrections

As every scattering experiment suffers from instrumental resolution and possibly scattering from other substances than the sample, these effects need to be taken into account and corrected for. One of the crucial correction is called the solid angle correction [59], and is a geometrical correction arising from the flat geometry of the detector. In scattering experiments the intensity over a solid angle is of interest. For a flat detector a solid angle will subtend a different number of pixels close to the beam center compared to far away from the beam center. Thus, to obtain the intensity over a solid angle this has to be corrected for.

Another important correction is for the bad pixels of a detector. They might be non-responsive, or giving an incorrect response to the detected intensity. These pixels are often masked out, so that they are not taken into account when integrating. The gaps between detector plates, appearing as black strips in fig. 4.1(a), together with the beam stop are usually also masked out in the same manner as the bad pixels.

In addition to the correction for bad pixels and solid angle, there is also a background correction originating from X-rays being scattered from other substances than the sample, e.g air, sharp edges [60]. This can be accounted for either before transforming the data from 2D to 1D by integration, or after. To subtract the background scattering from the diffraction pattern a separate measurement has to be preformed of only the background, including the capillary, to be subtracted from the diffraction pattern of the sample. The other possibility is to integrate the data first, and subsequently fit a background to the intensity and subtract it.

To compare results it is also important to normalize the data so that it is independent of acquisition time and beam current. This is usually achieved by dividing the intensity by the acquisition time and beam current. Depending on the type of experiment performed and the information wanted from the experiment, there are several more corrections that may be applied to the data [60, 59]. However, for the purpose of our measurements it is only necessary to take into account the corrections mentioned above.

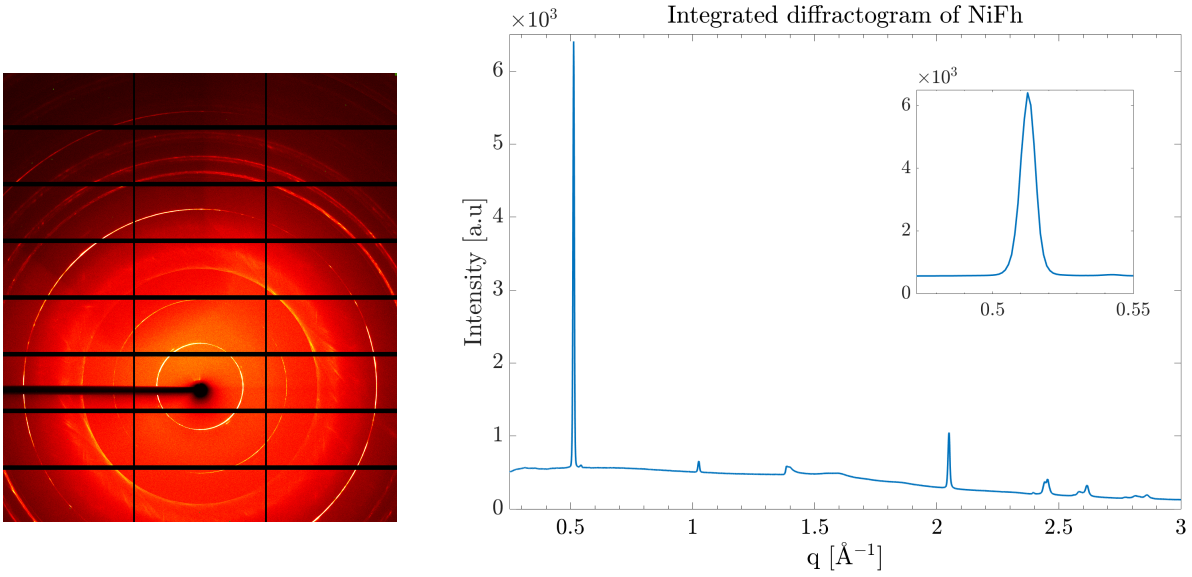

(a) (b)

Figure 4.1: (a) A typical diffraction pattern, gathered at the ESRF of NiFh. (b) The integrated intensity of the diffraction pattern in (a). Each peak corresponds to one ring on the diffraction image. The inset is a zoom in on the 001 Bragg peak of the integrated intensity, the innermost ring in the diffraction image.

4.3 Transforming 2D images to 1D data sets

To gain quantitative information from the diffraction patterns it is common to transform the diffraction pattern to a one dimensional data set. This transformation is done by performing integration of the diffraction image, summing up the intensities at each diffraction angle. There are more pixels in rings further out from the direct beam compared to close to the beam center. This is corrected for in the integration by binning pixels into groups of similar scattering angle and averaging the value of each bin [59]. Figure 4.1 displays an example of how the diffraction image and its integrated intensity profile looks like. At the ESRF the integration was performed automatically on site together with other corrections, making the further data treatment unnecessary [61]. While at the LNLS no data treatment was performed, and the data taken home to NTNU had to be integrated and corrected using the available software, DAWN Science [62].

4.4 Data extraction

ESRF data

After correcting and integrating the diffraction image, information about the sample could be extracted. As the goal of the experiments was to investigate the response of the clay when exposed to CO_2 at different temperatures and pressure, temperature and pressure are naturally two of the interesting parameters. Together with these also the time of the measurements, the peak positions and intensities are needed. A matlab program was made to extract all the necessary information from the images. The program acquires the temperature and time from the header of the diffraction image, while the pressure has to be manually entered for each file. Additionally the program finds all peaks using the built-in matlab function "findpeaks". The desired peaks are found through filtering out the other peaks by evaluating the prominence of the peaks. If

the prominence is greater than the mean prominence plus 0.1 times the standard deviations, it is stored for later use together with the intensity of the same point. The function that performs the finding and sorting of the peaks has been created by Barbara Pacáková. The detected peaks have also been visually inspected to ensure that no faults were made by the program. For unwanted peaks or undetected peaks these were removed or added manually.

LNLS data

Due to the setup of the experiment, the results from LNLS have a lower resolution compared to the ERSF data. The detector was placed very close to the sample, increasing the angular range, but decreasing the spatial/angular resolution. In addition, there was no rotation of the sample, decreasing the counting statistics and increasing the texture of the diffraction pattern, yielding relative intensities that might deviate from theoretical calculations [47]. However, the main goal of the measurements at LNLS was to investigate if the clays with different cations would absorb CO_2, and therefore only the position of the peak was considered. The data has been corrected for bad pixels and the solid angle as well as normalized to the exposure time of the measurements and beam current. A matlab program was created to subtract the background by fitting a third degree polynomial to regions of points between peaks in the data. The peak positions have been manually identified after plotting the integrated intensity.

5 Results

To study the intercalation and retention of CO_2 in the fluorohectorite clay, several experiments were performed. At the ESRF the Nickel-fluorohectorite was examined by measuring isotherms and isobars to determine at what temperature and pressure the CO_2 would enter and leave the interlayer. Another aspect of intercalation that was investigated was its the dependence on the cation. This was studied at the LNLS with the same procedure of exposing clays with different cations to CO_2, before heating to observe the retention properties. The cations used for this purpose were Li^+, Na^+, Ba^{2+}, Ca^{2+} and Cs^+, which have different charges and sizes that may both affect the intercalation properties of the clay.

In order to investigate these intercalation properties, X-ray diffraction has been utilized. The changes in the clay structure as it expands in contact with CO_2, manifests itself as a change in the position of the diffraction ring originating from the planes perpendicular to the stacking direction of the clay. Thus, this change can be related to a change in the distance between the platelets. The basal spacing, which is the distance from the top of one platelet to the top of the adjacent platelet, is often used to quantify the expansion of the clay. Calculations of the basal spacing are done by combining the results of Bragg and Laue, obtaining an equation for the basal spacing,

$$d = \frac{2\pi}{q},$$

where q is the magnitude of scattering vector and d is the basal spacing, also known as the d-spacing.

5.1 Results from ESRF

Nickel-fluorohectorite
To determine the pressure necessary for intercalation, the sample was exposed to different pressures at a temperature of 300 K. The pressure increase was performed in small steps, and kept at each step for approximately 1 h, or until no dynamics were seen. In addition to this, the temperature for intercalation at 1 bar was determined by cooling the sample from 300 K to 203 K, while keeping the pressure constant at 1 bar. Furthermore, the retention of the CO_2 in the clay was observed by heating the sample from 203 K to 400 K at 1 bar. A heating experiment was also performed at 13 bar, heating the sample from 223 K to 423 K. Moreover, an experiment probing whether the phase of CO_2 had any impact on the intercalation was conducted. The sample was then exposed to CO_2 in the liquid phase as well as in gas phase.

5.1.1 NiFh at 300 K exposed to 0 - 40 bar CO_2

The NiFh-sample was dried under vacuum in a 0.3 mm capillary by heating it to 400 K. The temperature was then reduced to 300 K and the sample was purged with CO_2 to remove any excess water. A measurement of the initial dry state was performed to assure that it was dry. The pressure was then increased in steps of 2 bar from 2 bar to 14 bar, before two larger steps were applied from 14 bar to 20 bar and further on to 40 bar. The pressure steps are displayed as separate colors for each pressure in fig. 5.1, and the color bar indicates the pressure that each color represent. To accurately determine the pressure at which the transition from zero CO_2 layers to one CO_2 layer occurs, the sample was kept at the same pressure for approximately 1 h, depending on whether any dynamics were observed. The time at each pressure can be seen from the inset of fig. 5.2(b), showing the pressure as a function of time.

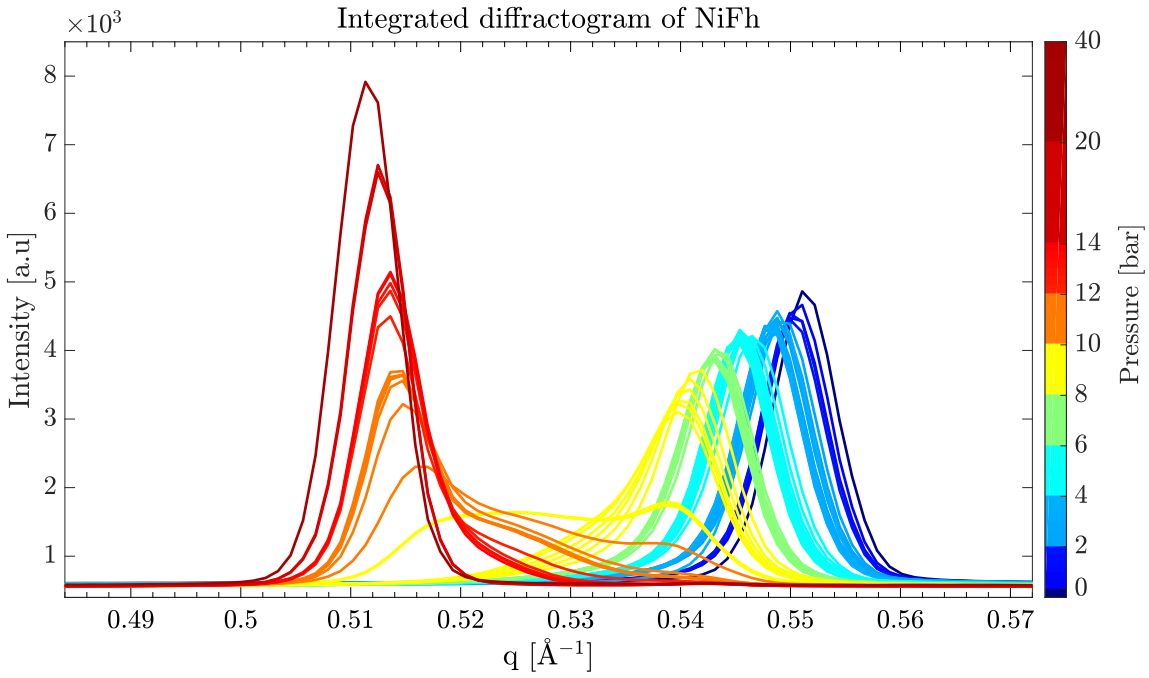

Figure 5.1: The integrated diffractogram of NiFh showing the development of the peak as pressure is increased from 0 bar to 40 bar at 300 K, as a function of the scattering vector, q.

Figure 5.1 shows how the 001 Bragg peak moves as the sample is exposed to pressures from 0 up to 40 bar. Initially the peak position is at q = 0.5511 $Å^{-1}$ (dark blue curve in fig. 5.1), corresponding to a basal spacing between the clay platelets of 11.40 Å, as expected for a dry, collapsed structure of NiFh [17]. As the pressure increases, the peak gradually moves towards lower q-values, e.g larger basal spacing (fig. 5.2(a)), suggesting that CO_2 started to intercalate between the clay platelets.

At pressures below 10 bar (yellow curves), the peak moves without any appreciable change in shape, or development of a pronounced shoulder. The only apparent change, except from the change in position, is the decrease in intensity. However, the decrease in intensity is expected as the intercalation initially creates a more disordered system. In contrast to this, larger changes are happening once the pressure reaches 10 bar. A large shoulder starts to develop to the left of the peak, around 0.520 $Å^{-1}$, indicating the onset of larger structural changes in the clay. The shoulder progresses until the peak becomes a double peak type with contributions from a third peak. The positions of the two main peaks are 0.5386 $Å^{-1}$ and 0.525 $Å^{-1}$, suggesting two dominant states in the clay.

When increasing the pressure to 12 bar, the double peak to changes. Observing the orange curves for 12 bar in fig. 5.1, it is evident that the first curve consists of contributions from three peaks. The intensity of the left peak at 0.512 $Å^{-1}$ increases, while the right and middle peaks at 0.5386 $Å^{-1}$ and 0.525 $Å^{-1}$ respectively, decreases. This development continues until there is only a small shoulder to the right of the peak at 0.5147 $Å^{-1}$, and the transition from one state to another has occurred. From fig. 5.2(c) it can be seen that the intensity at 12 bar recovers to the level before the transition at 10 bar. In addition to the increase in intensity of the peak, its position also shifts slightly towards lower q, as is evident in fig. 5.2(b), showing an increase in basal spacing at 12 bar. In fig. 5.2 the black lines represent a boundary between the dry state and intercalation of one layer of CO_2. This is only for visual demonstration and it not suggesting a hard boundary between dry and one layer of CO_2.

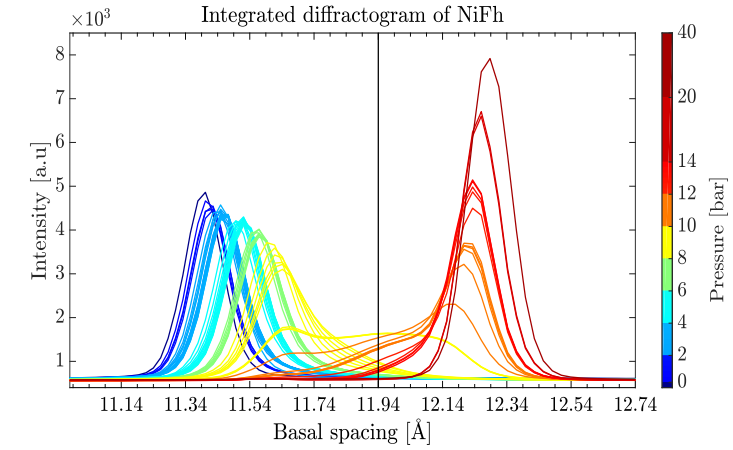

(a)

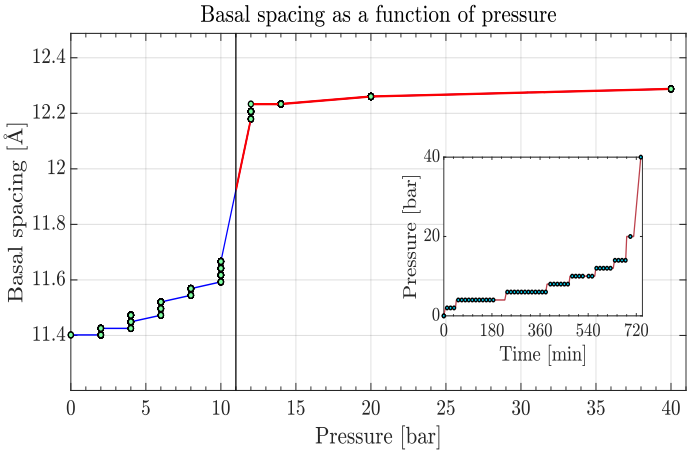

(b)

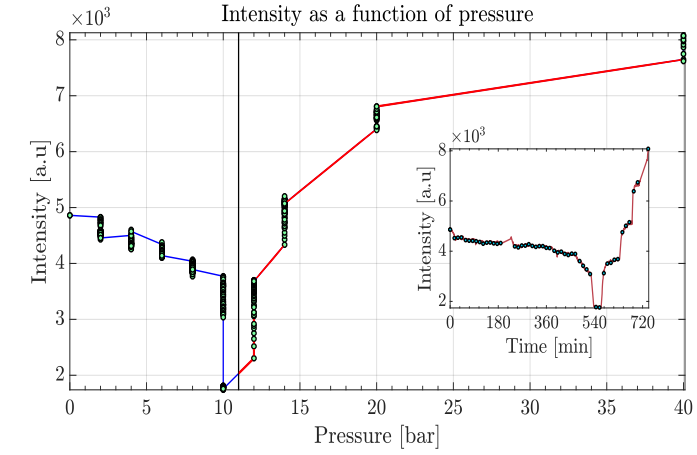

(c)

Figure 5.2: (a) The integrated diffractogram showing the development of the peak as pressure is increased from 0 to 40 bar at 300 K as a function of basal spacing. The vertical black line separates the dry region and the region of one layer CO_2 intercalated. Similarly for (b) and (c). (b) The basal spacing as a function of pressure calculated from the position of the peak. Inset of pressure as a function of time. (c) The development of the intensity of the 001 Bragg peak both before (blue curves) and after (red curves) the transition, as a function of pressure. Inset of intensity as function of time.

The transition is fast, ≈ 16 min, as can be seen from the inset of fig. 5.2(c), with a change in basal spacing of about 0.5 Å. Comparing the intercalation below 12 bar with the transition it is clear that the intercalation below 12 bar is very slow with a change of only ≈ 0.2 Å in 9 hours.

As pressure increases to 14 bar, the peak moves towards lower q and the intensity increases as the shoulder decreases. This increase in intensity is quite rapid and large, as fig. 5.2(c) shows. The intensity exceeds the intensity of the dry peak at 14 bar. At 20 bar the shoulder has vanished, the position has changed and the intensity has increased further. The same is the case when increasing pressure to 40 bar. The final position of the peak is at 0.5113 $Å^{-1}$ (12.29 Å).

5.1.2 NiFh cooled from 300 K to 203 K at 1 bar

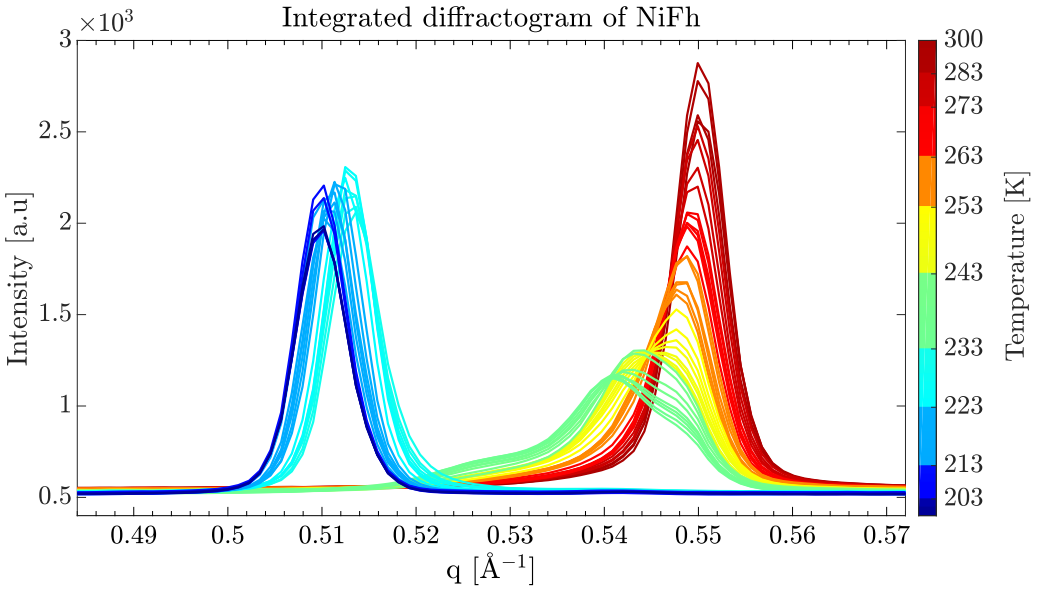

Figure 5.3: The integrated diffractogram showing the development of the peak as temperature is decreased from 300 K to 203 K at 1 bar as a function of the scattering vector, q.

The same sample was used for this experiment as for the previous experiment. After the exposure of the NiFh sample to 40 bar of CO_2, the sample was vented to release the CO_2. Subsequently, vacuum was pumped on the sample and it was heated to 400 K to remove any remaining CO_2. When the sample was dry at 400 K, the temperature was lowered to 300 K. A pressure of 1 bar CO_2 was then applied before initiating the measurements. The inset of fig. 5.4(b) shows how the temperature was changed. The sample was initially cooled from 300 K to 283 K in the first step, and afterwards in steps of 10 K, keeping the temperature constant for about 1 h at each step.

Looking at fig. 5.3, some of the same features as for the increase in pressure in fig. 5.1, can be recognized. The 001 peak moves slightly to lower q without changing its shape, but it decreases its intensity in a step-wise fashion at each temperature step, as can be seen in fig. 5.4(c). The steady movement of the peak continues until the temperature reaches 253 K. At 253 K the shoulder that initially developed at 263 K progresses, and the main peak becomes much broader. Decreasing the temperature to 243 K leads to a change in the broad peak, and two shoulders are distinguishable. One shoulder to the left at 0.5284 $Å^{-1}$ and one to the right (0.5477 $Å^{-1}$) of the main peak at 0.5408 $Å^{-1}$. From fig. 5.3 and fig. 5.4(c) it can be seen that the intensity also reaches its minimum at this temperature.

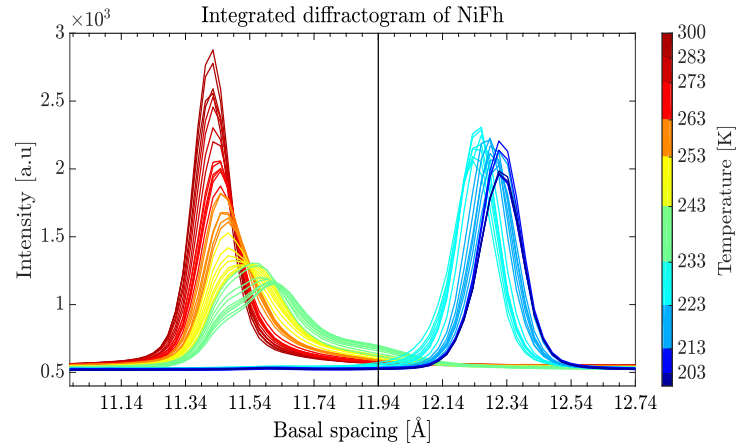

(a)

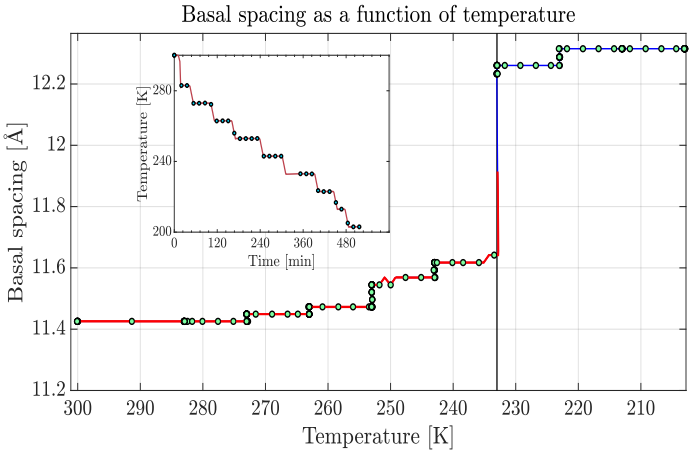

(b)

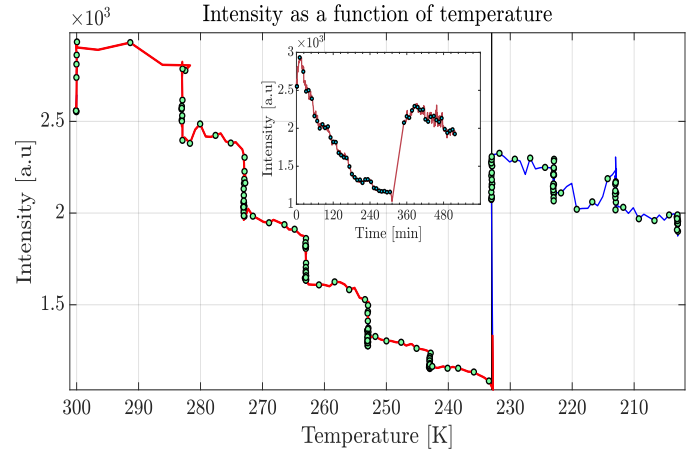

(c)

Figure 5.4: (a) The integrated diffractogram showing the development of the peak as temperature is decreased from 300 K to 203 K at 1 bar as a function of basal spacing. The vertical black line separates the dry region and the region of one layer CO_2 intercalated. Similarly for (b) and (c). (b) The basal spacing as a function of pressure calculated from the position of the peak. Inset of pressure as a function of time. (c) The development of the intensity of the 001 Bragg peak both before (red curves) and after (blue curves) the transition, as a function of pressure. Inset of intensity as function of time.

Noting that all figures in fig. 5.4 show an abrupt step at 233 K, it is necessary to mention that unfortunately the beam was dropped at this temperature, preventing the observation of the dynamics as the transition ocurred. Thus, the abrupt changes in basal spacing/peak position and intensity are artifacts of the missing information about the transition. However, it can be deduced that this transition happened relatively fast, $\approx$ 44 min or less, as this is the time period which lacks measurements. Also, from fig. 5.4(b) it can be seen that during the cooling from 243 K to 233 K the basal spacing remains constant, but increases when the temperature reaches 233 K.

From fig. 5.4(b) and fig. 5.4(c) it can be seen that both the intensity and basal spacing/peak position change at 233 K. As temperature is lowered further, the position of the peak changes to lower q and the intensity seems to be decreasing, but the shape remains the same. In contrast to the previous experiment, the intensity after the transition for this sample does not exceed the intensity of the initial state at 300 K. The resulting basal spacing is 12.32 Å.

5.1.3 NiFh heated from 203 K to 400 K at 1 bar

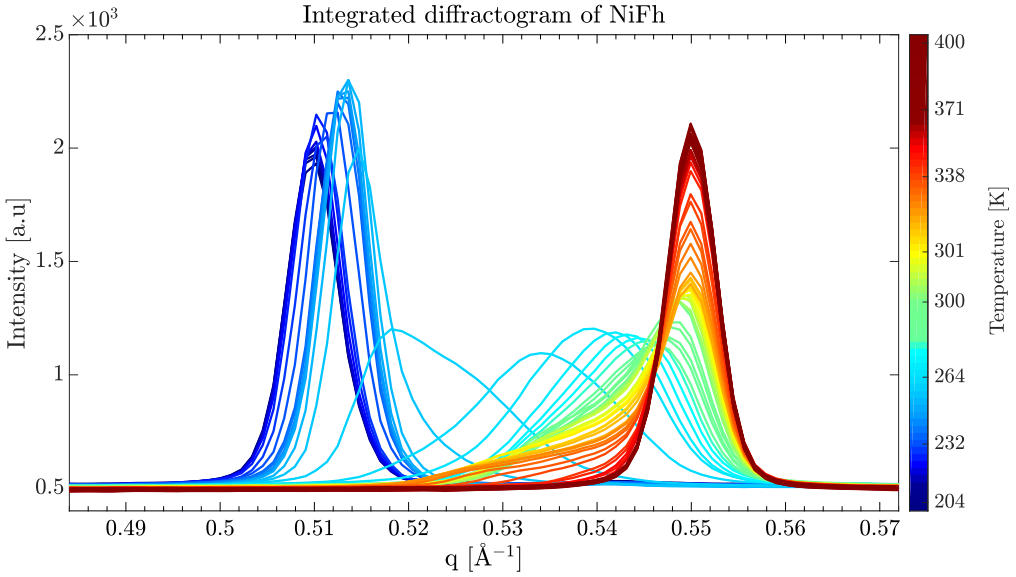

Figure 5.5: The integrated diffractogram showing the development of the peak as temperature is increased from 203 K to 400 K at 1 bar as a function of the scattering vector, q.

Having cooled the sample to 203 K at 1 bar so that the critical temperature for intercalation could be determined, the sample now initially contains one layer of CO_2. As it is equally interesting to examine the temperature for which the CO_2 leaves the interlayer, a heating experiment of the same sample at 203 K was performed. From the inset of fig. 5.6(b) it can be seen that the temperature increase is linear up to 300 K, where a plateau is reached before raising the temperature to 400 K. The heating rate was set to 100 K h^{-1}.

As the temperature starts to increase, the peak moves to higher q and its intensity increases. Following this increase in intensity there is a drastic and rapid drop at the onset of the transition. The inset of fig. 5.6(c) shows how rapid this drop occurs. The time from maximum to minimum intensity is about 8 min, and the magnitude of the drop is of the order of 10^3. The transition happens at a temperature of $\approx$ 263 K, which is higher than the temperature for intercalation of 233 K. This indicates a hysteresis behavior, where there is retention of the CO_2 beyond the conditions for intercalation.

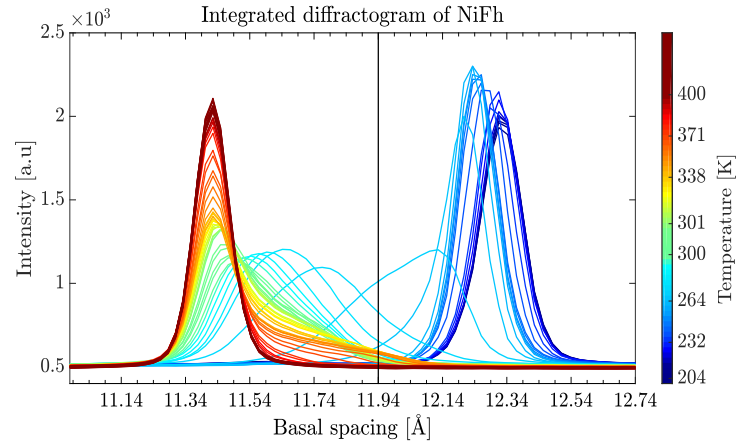

(a)

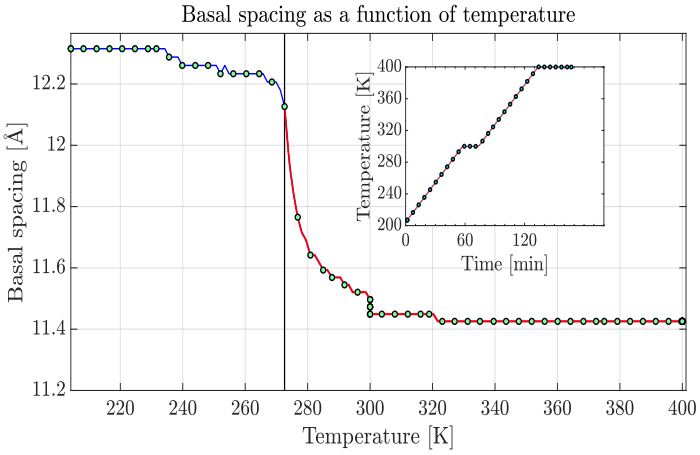

(b)

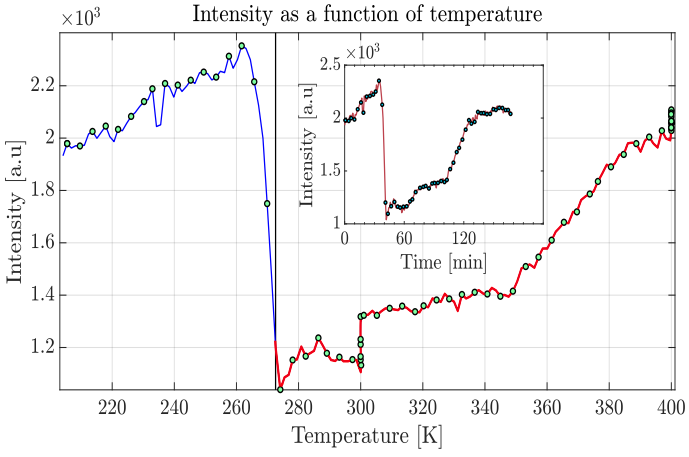

(c)

Figure 5.6: (a) The integrated diffractogram showing the development of the peak as temperature is increased from 203 K to 400 K at 1 bar as a function of basal spacing. The vertical black line separates the dry region and the region of one layer CO_2 intercalated. Similarly for (b) and (c). (b) The basal spacing as a function of pressure calculated from the position of the peak. Inset of pressure as a function of time. (c) The development of the intensity of the 001 Bragg peak both before (blue curves) and after (red curves) the transition, as a function of pressure. Inset of intensity as function of time.

Figure 5.5 shows how the peak changes in response to the temperature increase. To begin with, the movement of the peak is similar to the previous experiment, it moves without changing shape. At the onset of the transition the peak shape is broad with a large shoulder to the right (cyan blue curve). Subsequently, the peak temporarily recovers a symmetric shape, before the intensity increases and the peak moves to higher q, leaving a broad shoulder to the left of the peak (yellow curves). As the temperature increases further, the shoulder diminishes as the intensity increases. However, the position of the peak as the intensity increases does not change, as has been observed in the previous experiments, and remains at 0.5499 $Å^{-1}$ corresponding to 11.43 Å. In addition, the slowly recovering intensity (fig. 5.6(c)) does not exceed the maximum intensity before the transition, but rather stabilize around the same value as before the heating was applied.

The development of the peaks position can be seen in fig. 5.6(b), showing the basal spacing as a function of temperature. Looking at the basal spacing, an interesting behavior occurs during the transition. The spacing seems to be exponentially changing as a function of temperature. This suggests that as temperature is increased beyond the transition temperature, the de-intercalation is initially rapid until a certain point where most of the CO_2 has left the interlayer and the removal of the remaining CO_2 demands more energy.

Already at 300 K the peak position is close to the position of the dry state. However, a closer look at fig. 5.5 and fig. 5.6(c) reveals a broad peak with a large shoulder and low intensity. The shoulder starts to diminish as the intensity increases with higher temperature, and not until the temperature reaches 380 K is the intensity at the same level as pre-heating. As the temperature is kept at 400 K the intensity continues to increase, indicating that there might still be CO_2 in the sample, or a reorganization within the grains, producing a more ordered system.

5.1.4 NiFh exposed to 0 - 26 bar at 253 K

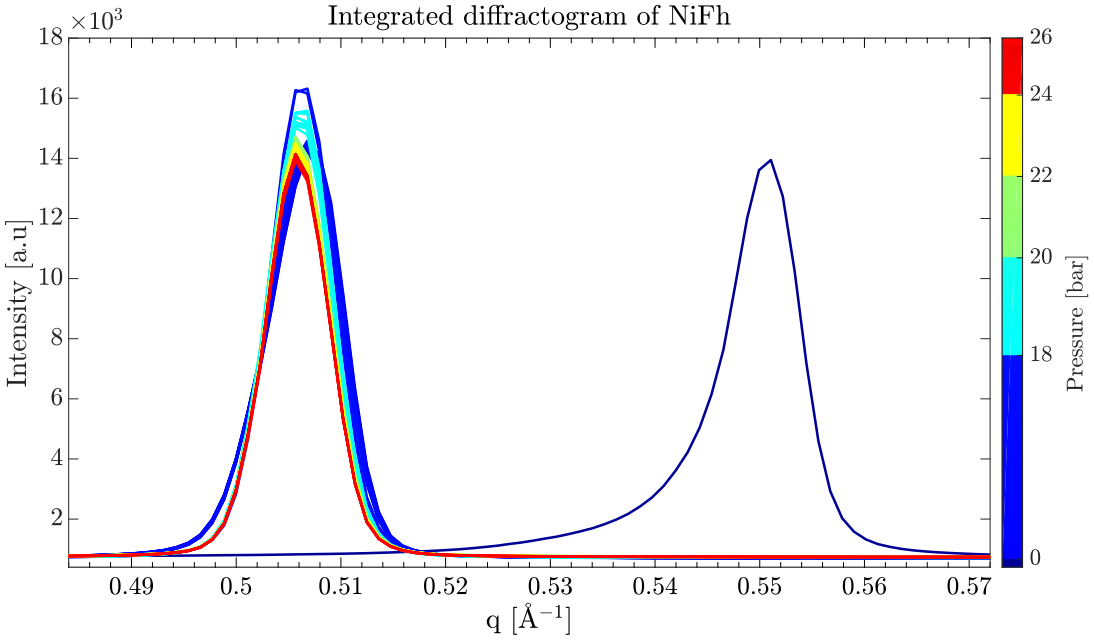

Figure 5.7: The integrated diffractogram showing the development of the peak as pressure is increased from 0 to 26 bar at 253 K as a function of the scattering vector, q.

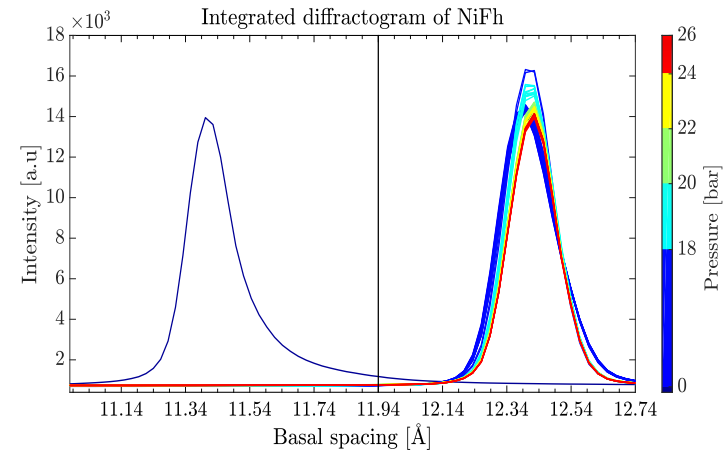

(a)

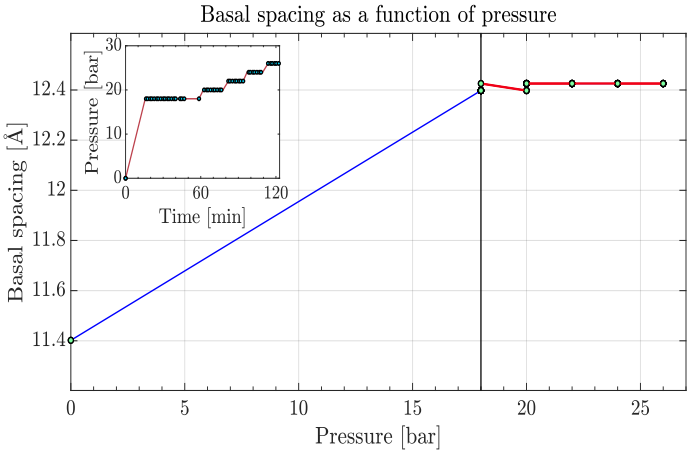

(b)

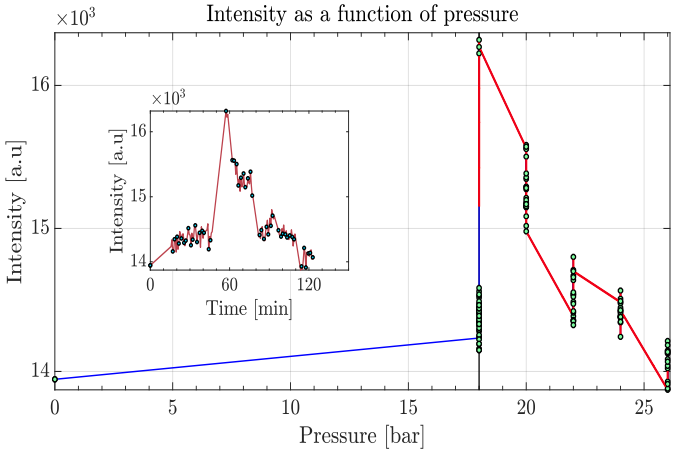

(c)

Figure 5.8: (a) The integrated diffractogram showing the development of the peak as pressure is increased from 0 to 26 bar at 253 K as a function of basal spacing. The vertical black line separates the dry region and the region of one layer CO_2 intercalated. Similarly for (b) and (c). (b) The basal spacing as a function of pressure calculated from the position of the peak. Inset of pressure as a function of time. (c) The development of the intensity of the 001 Bragg peak both before and after the transition, as a function of pressure. Inset of intensity as function of time.

For the three previous experiment the same sample of NiFh in a 0.3 mm capillary was used. For this experiment, a new sample was prepared in a 0.5 mm capillary. The sample was attempted dried for a long time at 400 K while pumping vacuum on it. It was also flushed three times with CO_2 to remove any water in the sample. However, neither of these things succeeded and the temperature was increased to 423 K. Once it looked dry at both 423 K and at 300 K the sample was cooled to 253 K. From fig. 5.7 the initial peak at 0.5511 $Å^{-1}$ shows a shoulder to the left, indicating that the sample was not completely dry. The reason for the difficulties in drying the sample properly may be due to the larger capillary used in this experiment. It was decided to continue the experiment, although the initial state was not completely dry.

After drying the sample and cooling it to 253 K, a pressure of 18 bar CO_2 was applied. Figure 5.7 and fig. 5.8(b) show that the transition from zero layers of CO_2 to one layer was immediate. Increasing the pressure in steps of 2 bar up to 26 bar does not further change the position of the peak. The only change is a decrease in the intensity of the peak (fig. 5.8(c)). However, it is interesting to note that the final basal spacing is about 12.43 Å, which is slightly larger than for the previous experiments. This may be a consequence of not drying the sample properly.

5.1.5 NiFh exposed to CO_2 in liquid phase

When the pressure was increased beyond 20 bar at 253 K, the CO_2 entered the liquid phase, as can be seen from the phase diagram of CO_2 in fig. 5.9. To investigate whether the pressure and temperature within the liquid phase had any effect on the intercalation, several different temperatures and pressures were applied. The sample was the same as for the previous experiment, and thus the initially conditions were 26 bar and 253 K. The sample was then cooled from 253 K to 223 K in steps of 10 K, before the pressure was changed to 13 bar. The different conditions of the liquid phase applied are highlighted in fig. 5.9. Figure 5.10 shows the peak as the CO_2 is in the liquid phase. No changes except from fluctuations in the intensity is visible.

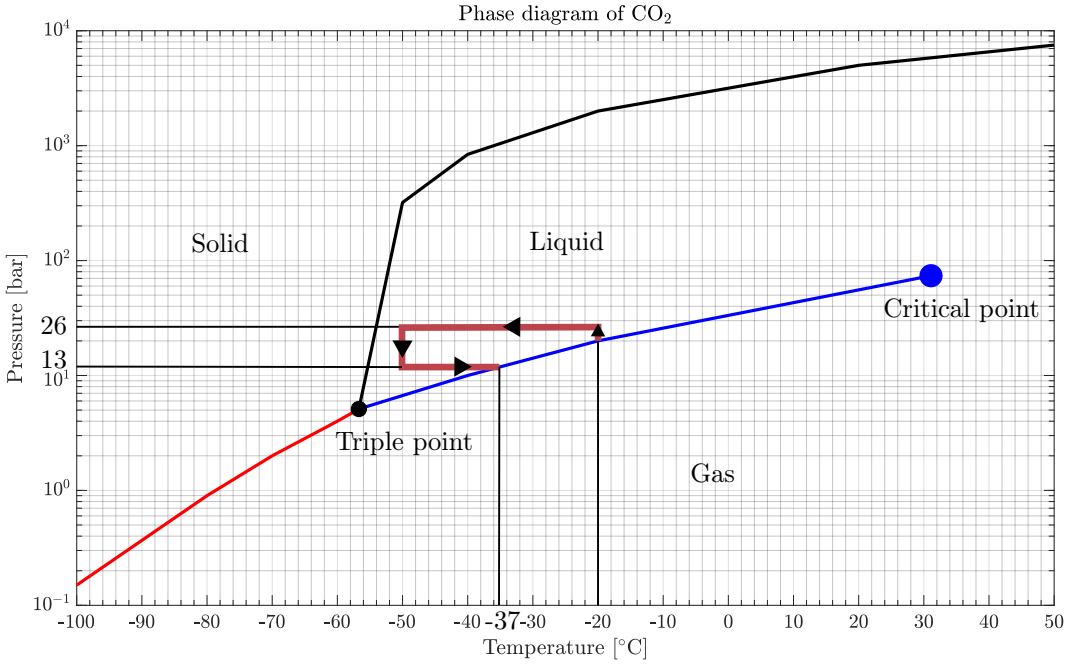

Figure 5.9: A rough phase diagram for CO_2 showing conditions for triple point, gas phase, solid phase and liquid phase [63]. It shows how the conditions were changed during the experiment.

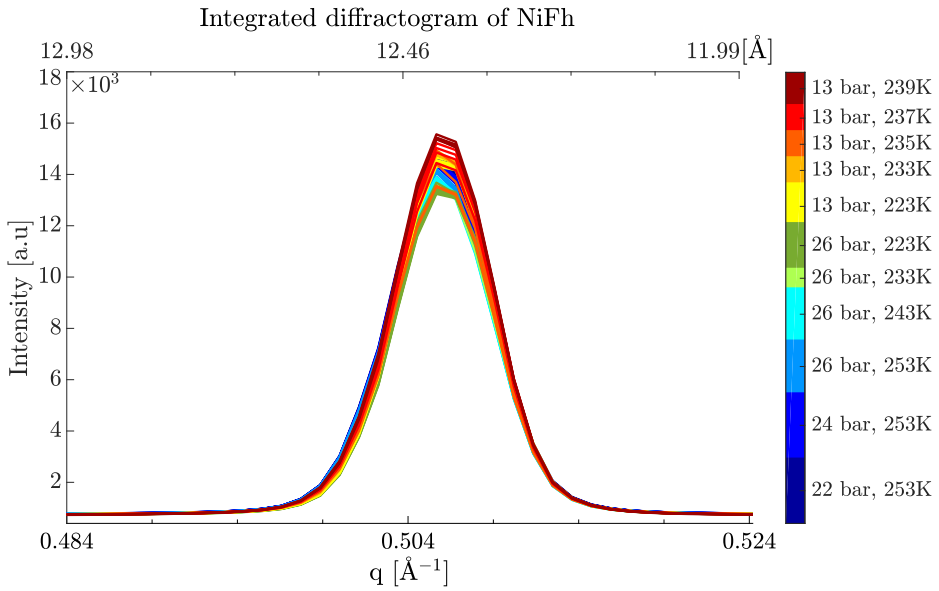

Figure 5.10: The integrated diffractogram showing the lack of development of the peak in the liquid CO_2 phase. Initial pressure and temperature was 26 bar and 253 K. Temperature was reduced to 223 K, before the pressure was reduced to 13 bar.

5.1.6 NiFh at 13 bar heated from 223 K to 423 K

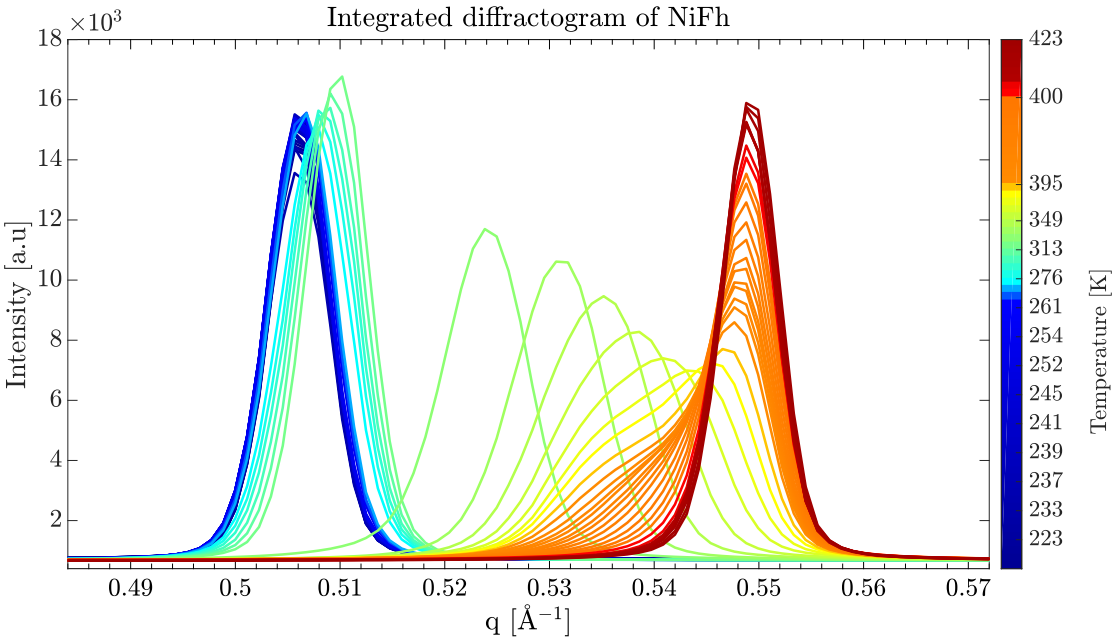

Figure 5.11: The integrated diffractogram showing the development of the peak as temperature is increased from 223 K to 423 K at 13 bar as a function of scattering vector, q.

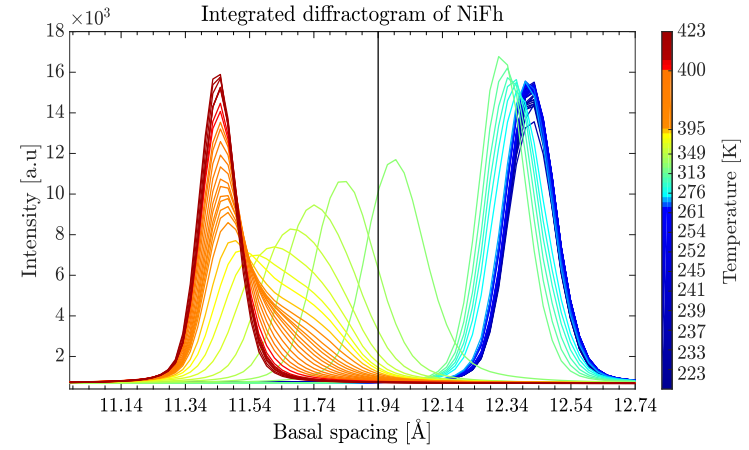

(a)

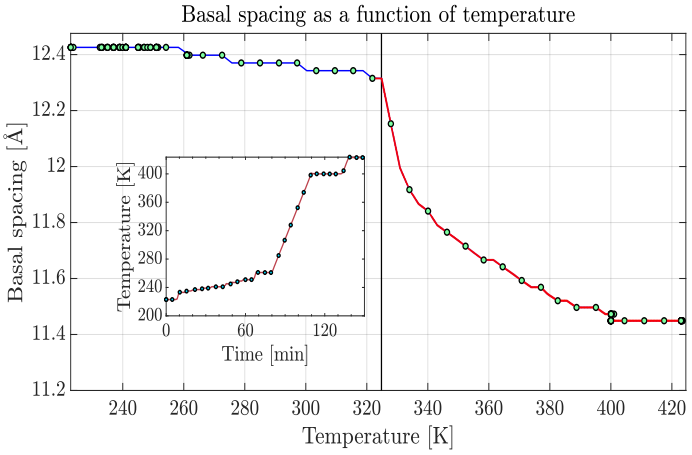

(b)

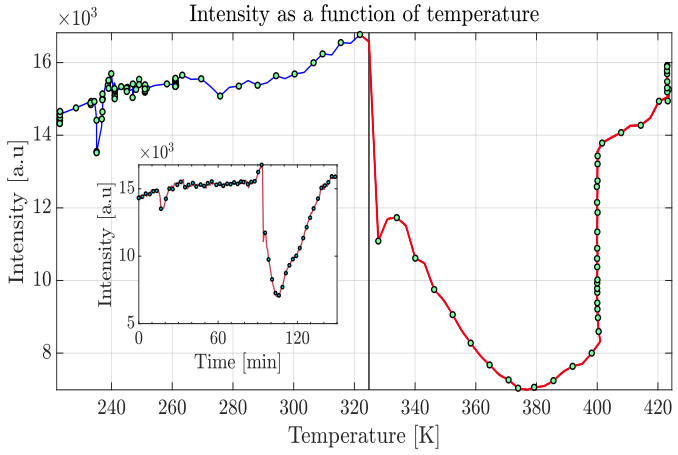

(c)

Figure 5.12: (a) The integrated diffractogram showing the development of the peak as temperature is increased from 223 K to 423 K at 13 bar as a function of basal spacing. The vertical black line separates the dry region and the region of one layer CO_2 intercalated. Similarly for (b) and (c). (b) The basal spacing as a function of pressure calculated from the position of the peak. Inset of pressure as a function of time. (c) The development of the intensity of the 001 Bragg peak both before and after the transition, as a function of pressure. Inset of intensity as function of time.

As no major changes were observed in the two previous experiments, the sample was subjected to a heating process at a pressure of 13 bar, to investigate when the CO_2 leaves the interlayer. The sample was first heated from 223 K to 233 K, before being heated in steps of 2 K up to 251 K. From fig. 5.11 it can be seen that no major changes occurred in this temperature interval. As time was limited, the rate of heating from 261 K to 400 K was set to $280\,\mathrm{K\,h^{-1}}$.

Figure 5.11 shows that the peak displays similar dynamics as previous experiments, namely moving without changing shape. As the temperature was raised above 323 K, the transition begun (fig. 5.12(b)). The peak decreases rapidly in intensity as seen in both fig. 5.11 and fig. 5.12(c), and simultaneously the peak moves and broadens. Close to 350 K the peak becomes asymmetric, developing a large shoulder that remains as the temperature was further increased. Only while the temperature was kept at 400 K does the shoulder decrease to nothing.

Looking at fig. 5.12(b), it exhibits the same feature as in fig. 5.6(b), with a shape of exponential decrease in basal spacing. For both heating procedures the increase in temperature was linear, but of different heating rates. In addition to this, the development of the intensity is also similar for the two cases. The drop in intensity from maximum to minimum happens in ≈ 15 min, and after the minimum, the intensity increases to the same level as for the initial state.

5.2 Results from LNLS

To study how the cation affects the absorption of CO_2 in the clay, several experiments were performed with clays of different cations. The cations chosen were Li^+, Na^+, Ba^{2+}, Ca^{2+} and Cs^+. Figure 5.13 displays the periodic table with the radii of the neutral atoms, and their ionic radius marked by the dark gray color. The cations used in these experiments are marked with red boxes. From this it can be seen that Cs^+ and Ba^{2+} are quite large, while Li^+, Ca^{2+}, and Na^+, are a bit smaller. However, it should be noted that Ni^{2+}, that was used for the experiments at ESRF, was the smallest of all the cations that were investigated.

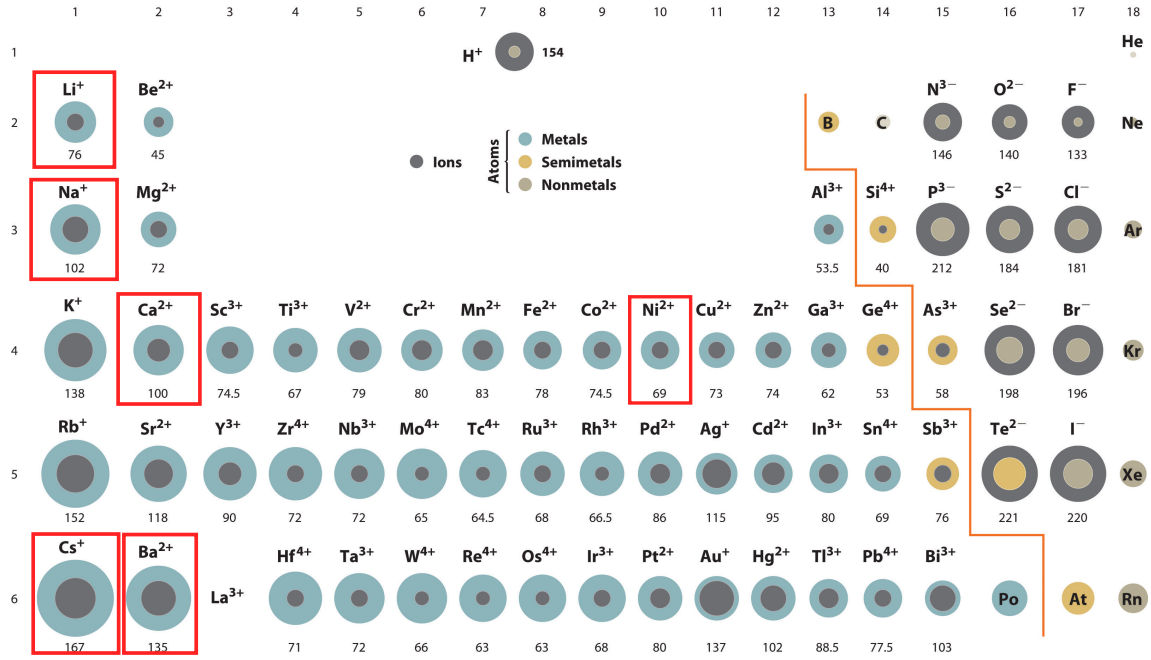

Figure 5.13: Figure showing the atomic and ionic radii of different ions. The dark gray is the ionic radius, and the number beneath every ion is the ionic radius in picometres. Other colors represent the neutral atomic radius. Adapted with permission from ref.[64]

The procedure that was used for all the experiments performed at LNLS was developed to investigate whether the clay absorbed CO_2 or not, and if it did, at what temperature the CO_2 would be released at 1 bar. The first step was to dry the clay properly under vacuum. This was done by heating the sample to 423 K with the cryojet until the peak position and shape indicated that the sample was dry. As a check of the dryness, the sample was cooled to 300 K. If the sample was still dry at this temperature, it was cooled down further to 253 K. A measurement at 253 K was performed before exposing the sample to 20 bar of CO_2. The sample was kept at 20 bar and 253 K for at least 1 h, or longer depending on whether any dynamics were observed. Subsequently, the pressure was increased to 50 bar and kept there for about 1 h. After no changes were observed at 50 bar the pressure was reduced to 1 bar and kept there until no changes were observed. The sample was then heated from 253 K to 403 K. The rate of heating was determined based on the intercalation dynamics observed as pressure was increased.

5.2.1 Lithium-fluorohectorite

One of the clays that was probed was the Lithium-fluorohectorite. Previous studies of LiFh clay have shown that it tends to absorb CO_2 [23, 26]. However, those studies use a different LiFh clay purchased from Corning.Inc. It is therefore interesting to see whether the Bayreuth clay [44] possess different intercalation properties compared to the Corning clay.

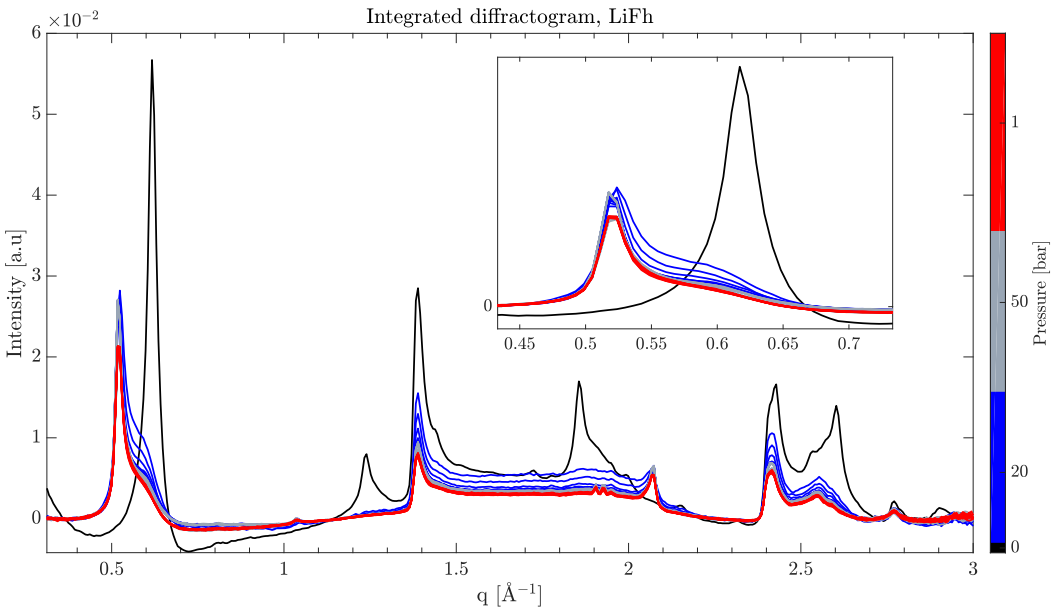

Figure 5.14: Integrated diffractogram of LiFh exposed to 0 bar, 20 bar, 50 bar and 1 bar at 253 K. The color bar shows the different pressures represented by each color, and the inset is a zoom in on the 001 Bragg peak.

Figure 5.14 shows the response of the LiFh to 20 bar, 50 bar and 1 bar at 253 K. The initial dry 001 Bragg peak before exposure to CO_2 (black curve) lies at a q-value of approximately 0.617 $Å^{-1}$, corresponding to a basal spacing of 10.2 Å. This basal spacing is about 1 Å smaller than for the dry NiFh. As pressure was increased to 20 bar, the 001 peak had moved to lower q before measurement was started, which was approximately 8 min after the pressure was increased. The position of the 001 peak after the intercalation is 0.517 $Å^{-1}$ or a basal spacing of 12.2 Å, an increase of 2 Å. However, there is still a broad shoulder to the right of the peak which only slightly diminishes over time. As pressure was increased to 50 bar, and decreased again to 1 bar, no significant changes were observed.

As the temperature was increased slowly from 253 K and up to 403 K the peak moved back towards its original position. From fig. 5.15 it can be seen that the peak starts to move as the temperature increases to 268 K (cyan colored curves), and the movement continues as the temperature increases further. The time from starting the heating and until the peak was back at its original position at 403 K, was $\approx$ 150 min.

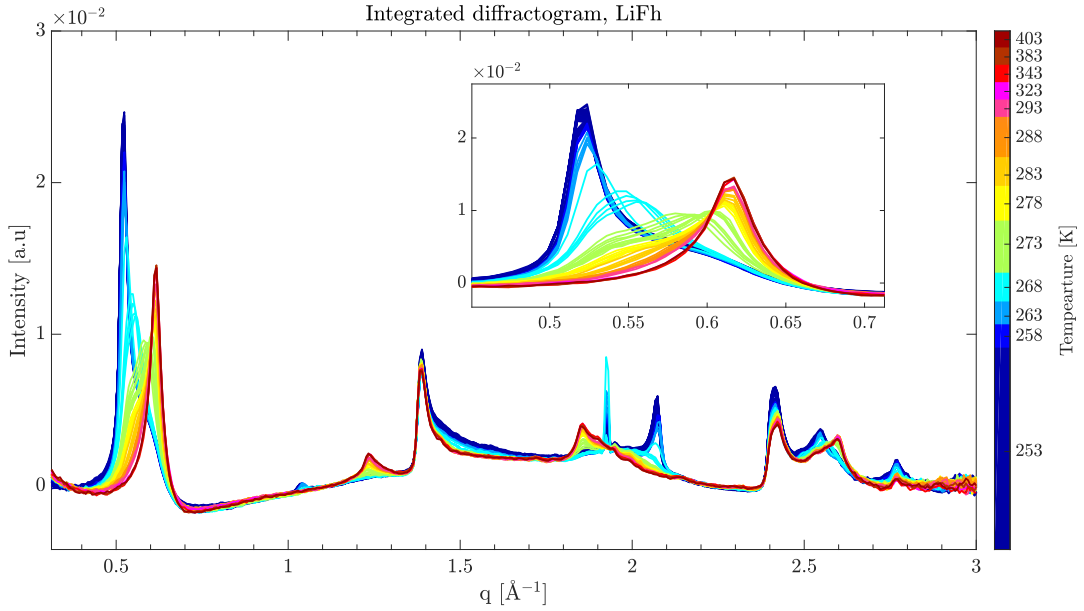

Figure 5.15: Integrated diffractogram of LiFh showing the response to heating from 253 K to 403 K at 1 bar. The color bar shows the different temperatures represented by each color, and the inset is a zoom in on the 001 Bragg peak.

5.2.2 Sodium-fluorohectorite

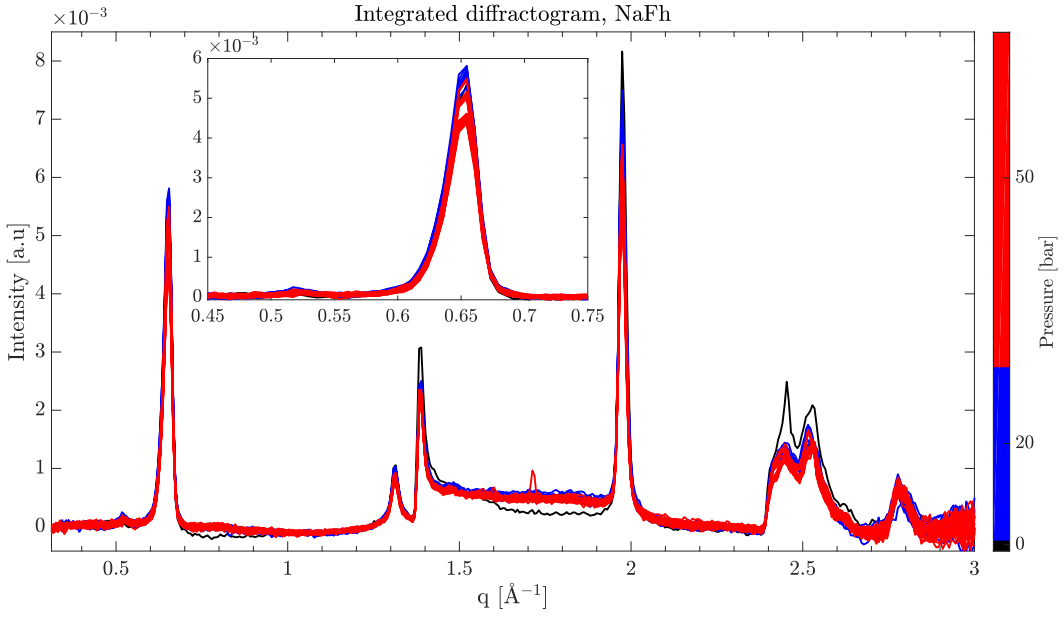

Figure 5.16: Integrated diffractogram of NaFh exposed to 0 bar, 20 bar, 50 bar. The color bar shows the different pressures represented by each color, and the inset is a zoom in on the 001 Bragg peak.

As for the lithium-fluorohectorite, the CO_2 absorption in Corning Inc. Sodium-fluorohectorite has also been studied before. Two of the studies, by Michels et al. and Hemmen et al., both found that NaFh shows very slow intercalation dynamics when exposed to CO_2 [23, 24]. However, the limited time frame of experiments performed on a synchrotron prevented the examination of such slow intercalation dynamics, and the same measurement procedure was used for NaFh.

In fig. 5.16 the black curve represents the sample before being exposed to CO_2, while the blue and red are the measurements of the sample exposed to 20 bar and 50 bar, respectively. From this it can be seen that a small peak appears at $\approx 0.517\,\text{Å}^{-1}$. This corresponds to a basal spacing of 12.2 Å, which indicates that CO_2 is intercalating into the clay. The 001 Bragg peak at $0.654\,\text{Å}^{-1}$, corresponding to a basal spacing of 9.6 Å, does not shift. Due to the difficulties in spotting the smaller peak, and the lack of movement of the peak at 9.6 Å, the sample was, at the time of the measurement, considered to not absorb CO_2, and the heating of the sample was omitted.

5.2.3 Barium-fluorohectorite

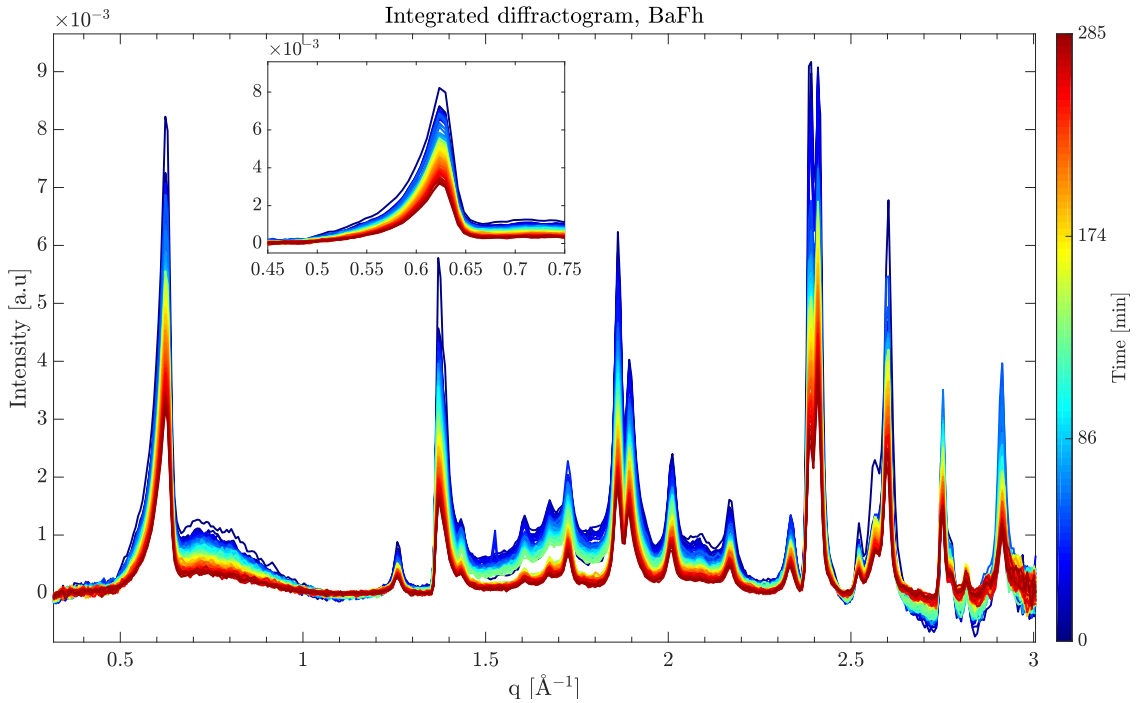

Figure 5.17: Integrated diffractogram of BaFh exposed to 0 bar, 20 bar, 50 bar, and heated from 253 K to 398 K at 1 bar. The colors serve to differentiate the curves from one another, and time increases from blue to red. The inset is a zoom in on the 001 Bragg peak.

Looking at fig. 5.17 it can be observed that the 001 Bragg peak is asymmetric with a shoulder to the left of the peak. This may suggest that the sample has not been completely dried by the heating. In spite of this, there is no change in the peaks position as it is exposed to 20 bar, nor for 50 bar or 1 bar. Even as the sample was heated from 253 K to 398 K no change is visible, and the peak stays at a position of $0.623\,\text{Å}^{-1}$, the basal spacing being 10.1 Å.

5.2.4 Cesium-fluorohectorite

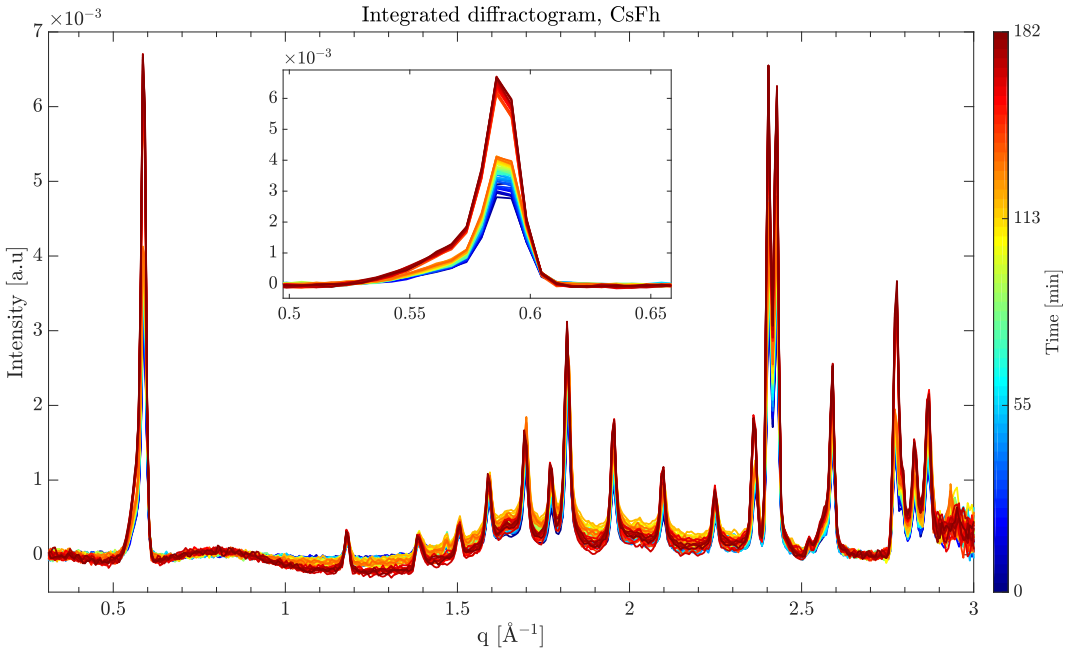

Figure 5.18: Integrated diffractogram of CsFh exposed to 0 bar, 20 bar and 50 bar, and heated to room temperature at 1 bar. The color bar represents the time development from the start of the measurement (blue) to the end (red). The inset is a zoom in on the 001 Bragg peak.

Measurements with the same procedure were also conducted with Cesium-fluorohectorite, which has the larges ionic radius of the cations used in these experiments. From fig. 5.18 it is evident that CsFh, similarly to BaFh, does not show any signs of intercalating CO_2 under any of the probed conditions. The 001 peak stays at the same position of 0.586 Å^{-1}, which means a basal spacing of 10.7 Å, during the whole measurement. The 001 peak appears asymmetric with a small shoulder to the left of the peak, which might suggest that the sample was not entirely dry.

During the heating of this sample the nitrogen for the cryojet unfortunately ran out, and so there was no controlled temperature increase. However, seen as no CO_2 seemed to be absorbed, this had no noticeable effect on the results.

5.2.5 Calcium-fluorohectorite

For Calcium-fluorohectorite a broad 001 double peak is seen before the exposure to CO_2, as the black curves in fig. 5.19 shows. This indicates that there may still be water inside the sample. As pressure was increased, the double peak disappears and becomes symmetric at a position of 0.604 Å^{-1}, corresponding to a basal spacing of 10.4 Å. As pressure was increased no change in the position was seen, and no intercalation of CO_2 occurred.

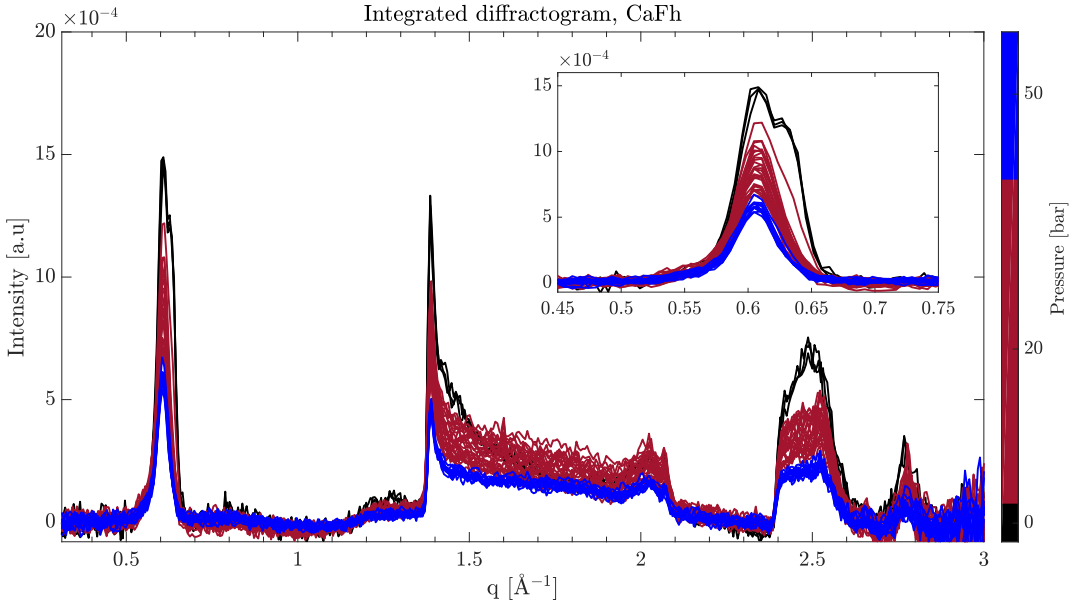

Figure 5.19: Integrated data of CaFh exposed to 0 bar, 20 bar and 50 bar. The pressures represented by each color are shown in the color bar. The inset is a zoom in on the 001 Bragg peak.

A summary of the different basal spacings for the clays of different cations is displayed below in table 3. The uncertainties have been manually found by examining a set of curves from each experiment. The difference between the two data points closest to the highest intensity point of the peak was found, and an average of those values were calculated and rounded up to the closest tenth.

Table 3: Table showing the basal spacing of the clays of different cations in dehydrated state and with one layer of CO_2 present.

Cation	Dehydrated [Å]	1 layer of CO_2 [Å]
Ni^{2+}	11.40 ± 0.06	12.43 ± 0.06 & 12.29 ± 0.06
Li^{+}	10.2 ± 0.3	12.2 ± 0.3
Na^{+}	9.6 ± 0.3	12.2 ± 0.6
Ba^{2+}	10.1 ± 0.3	—
Cs^{+}	10.7 ± 0.3	—
Ca^{2+}	10.4 ± 0.3	—

6 Discussion

6.1 Nickel-fluorohectorite

An interesting feature observed in most of the samples that intercalated CO_2, is the steady movement of the peak during absorption and release. Previous studies report a stepwise intercalation with discrete intercalation states of both water and CO_2 [24, 65]. However, the subtle, continuous movement of the peak suggests that the intercalation does not occur in jumps as CO_2 enters a layer. Instead, a possible explanation of this continuous intercalation of CO_2 may be that CO_2 enters different layers, expanding only part of it, resulting in a superpositioning of all the different spacings. It might also be due to mixed intercalation states [66], with some layers containing no CO_2, while others contain one layer of CO_2.

Reorganization and geometrical orientation of the CO_2 molecules within the layer may also contribute to the basal spacings being inconsistent with the reported stable states. For the Nickel-fluorohectorite samples investigated at ESRF, the interlayer distance (distance between top and bottom of two adjacent platelets) is approximately 2.3 Å. A CO_2 molecule is linear and its length is around 2.32 Å, ruling out vertical alignment within the layer. To support this, several molecular dynamic simulations and nuclear magnetic resonance (NMR) measurements have been performed, showing that the CO_2 molecules will usually orient themselves parallel to the clay surfaces [67, 68, 68, 25, 42]. This can not be determined from the measurements conducted here, but for future experiments, measurements such as infrared, Raman, or NMR spectroscopy could convey useful information on the continuous intercalation behavior and orientation of CO_2 within the layers. In fact, Raman spectroscopy was performed on some of the samples measured at the ESRF. However, the samples showed fluorescence, which prevented the collection of information on the vibrational modes of the molecules in the sample, and so, no analysis of the Raman data was executed. Curiously, the fluorescence was not present for samples containing water. Explanation of this phenomena is outside the scope of this work, but should be examined in future work to determine the origin of the fluorescence.

A study performed by Altoé et al. [17] has also revealed a continuous absorption phenomena for water in a different Nickel-fluorohectorite, similar to that observed for CO_2 in this work. They suggested two possible answers for this behavior; either mixed intercalation states, so called Hendricks-Teller states [66], or formation of Nickel- hydration complexes, or a combination of both. The analogue to the proposed Nickel-hydration complexes are CO_2-Nickel complexes. Formation of such CO_2-Nickel complexes have already been suggested by Michels et al. [23], who observed that the peak did not return to its initial dehydrated state when drying the sample after exposure to CO_2. Comparing the initial basal spacing of fig. 5.2(b) and fig. 5.4(b) it can be seen that the basal spacing in fig. 5.4(b) is slightly higher, about 0.03 Å, than the one for the dehydrated sample that had not been exposed to CO_2. However, this difference is within the uncertainty limits of ± 0.06 Å for the ESRF data, and thus is not significant. On the other hand, it is likely that the mixed intercalation states are the reason for the continuous intercalation dynamics. The peaks apparent continuous movement may be a construction of two peaks, representing different intercalation states, lying so close that they are observed as a single peak.

Even though the results of Altoé et al. [17] show similarities with the results obtained for Nickel-fluorohectorite in this work, direct comparison is not advisable due to the differences of the two systems. The Bayreuth clay [44] used for our experiment has a more homogeneous charge distribution. This can be argued by comparing adsorption isotherms of water for the Bayreuth NaFh and the Corning.Inc NaFh in refs.[43, 69]. The two adsorption isotherms both show a step from 1WL to 2WL. However, the Bayreuth clay is stable at a plateu of 1WL before a rapid transition to 2WL, while the Corning.Inc clay shows a more continuous increase in basal spacing at 1WL. This broader transition could indicate a larger charge distribution in the Corning.Inc clay [70]. In addition to the charge homogeneity of the clay, the difference between water and CO_2 should be considered. In fact, for the transition between dehydrated and one water layer, Altoé et al. observed a discontinuous transition for all the samples, whereas the results presented here showed a continuous transition.

As pressure was increased to 10 bar in fig. 5.1, the peak develops a large shoulder which progresses to become a double peak, with contribution from a third peak between the two main peaks. Such a transition peak was also observed for LiFh by Michels et al. [71]. However, the two main peaks in ref.[71] were located at positions representing definite intercalation states of 1, 1.5 and 2 water layers, whereas this is not the case for the double peak observed in fig. 5.1. Simultaneously, as the shoulder increases (yellow curves in fig. 5.1), the intensity of the peak decreases. This indicates that the population of the semi-stable state is decreasing and converting into another semi-stable state, represented by the emergence of the second peak. The double peak configuration develops between the two definite stable states of the dehydrated clay and the one CO_2 layer state. It might originate from a mixing state of the two states, as have been reported in previous works with H_2O hydrated clays [17, 18, 19].

On a side note, it is important to mention that the sudden development of the double peak is a bit of an artifact. During the measurement at 10 bar, the sample was moved to a different position for a short period of time, before being returned to the original position. In this time, the peak which was developing a shoulder, turned into a seemingly stable double peak. The development of the double peak might have been induced by a change in temperature, as the focusing point of the cryostream changed when the sample was moved. However, it is also possible that the development of the double peak would have taken place either way. Equivalently, part of the the sudden drop in intensity at 10 bar in fig. 5.2(c) is also an artifact.

The transition from one state to another, initiated at 10 bar, developed fully as the pressure increases to 12 bar. From fig. 5.1 it can be seen that the contributions to the intensity now consists of three peaks. Two of them are positioned at the same scattering vector as before the transition, but the third, and now main peak, is more to the left, indicating an increase in basal spacing. The rapid transition suggests that an energy barrier for intercalation into a one CO_2 layer like state exists, and that it is breached around 12 bar and 300 K. Such an energy barrier has been predicted for a similar clay species, montmorillonite, with different cations by molecular dynamics simulations [72, 25]. However, due to its similarity with the hectorite clay it is reasonable to assume that the results also apply to hectorite. On the other hand, the size of this energy barrier might differ depending on the cation, as different charge and size affects the intercalation dynamics [42]. The same type of energy barrier for absorption of CO_2 has also been discussed by Michels et al. [23], and experimental results are in agreement with the prediction of an energy barrier.

Comparing the curves right before and after the transition of fig. 5.1 and fig. 5.3, it is clear that they show the same initial increasing shoulder before the transition. Additionally, the development of the transition peak in fig. 5.3 (green curves) has some resemblance to the curve after the transition in fig. 5.1 (orange curves), both having contributions from three peaks, creating broad shoulders. There is also the same continuous movement of the peak before the transition. Even the transition times of ≈ 16 min and >44 min are comparable. All these resemblances may indicate that the intercalation dynamics induced by both pressure and temperature are the same, as suggested in ref. [23].

Although there are many similarities between fig. 5.1 and fig. 5.3, there are also some differences. One such difference is the point at which the peak starts broadening and developing a shoulder. For the sample that was cooled, the peak starts developing a shoulder at a basal spacing of 11.47 Å, while the one for increasing pressure does not develop a shoulder until 11.59 Å, a difference of about 0.12 Å. It is difficult to determine exactly what causes this difference, and whether it is due to an intrinsic physical property related to the temperature, or if it is a coincidence, as there are no other measurements to compare with. However, two possible reasons for this may be the packing of the powder or residual CO_2 or H_2O. The samples were measured at different position in the capillary, and so the grains may be more available to the CO_2 molecules at one position compared to the other. Another factor that could induce further intercalation at a lower basal spacing is strongly bound residual molecules between the layers. It is not unreasonable to assume that molecules being strongly bound in the interlayer have overcome a large energy barrier to intercalate into the clay, lowering the barrier for other CO_2 molecules to enter. In addition to this, the thermal activity is damped at lower temperatures, which might also enhance the capture of CO_2 [23].

Looking at the relative intensities of the dehydrated peak and the one CO_2 layer peak in fig. 5.1, it can be seen that the intensity of the peak at 12.42 Å (one CO_2 layer) is larger than the dehydrated peak. This is as expected as both the structure factor and Lorentz-polarization factor have increased contributions to the intensity at lower q values. In contrast to this, the intensity of the dehydrated and one CO_2 layer peaks of fig. 5.3 and fig. 5.5 show the opposite, namely that the intensity of the dehydrated peak exceeds that of the one CO_2 layer peak. A possible reason for this is a misalignment of the capillary. As the capillary was moved to measure at a different position it was not realigned at this position. Thus, during the rotation of the capillary the beam might have hit the capillary edges or closer to the edges at one part of the rotation and in the center of the sample at other parts, producing the observed intensity. Similar relative intensities are also observed for fig. 5.7 and fig. 5.11.

Another feature of fig. 5.3 is the decrease in intensity as the temperature is decreased after the transition. The converse is visible for the case of heating the sample in fig. 5.5, where the intensity increases as the temperature increases. These changes are probably due to the increased density of the CO_2 as the temperature is decreased, causing higher attenuation of the X-rays, reducing the scattered intensity. Previously, Fripiat et al. showed that the intensity of the 001, 002 and 003 reflections decreased in CO_2 atmosphere as temperature was decreased, in line with what is observed here [73]. They also probed whether the temperature itself was the cause of this decrease by lowering the temperature of an outgassed sample, which showed no evidence of altering the diffraction pattern. Similar decrease and increase in intensity of the one CO_2 layer peak is also visible in fig. 5.7 for increased pressure, and fig. 5.11 for heating the sample.

The rapid heating of the sample in fig. 5.3 conceals the intermediate steps of the continuous movement of the peak after the transition. The peak settles at the dehydrated position early, and a reduction of the shoulder, simultaneously as the peak intensity increases, is visible. A similar behavior is also seen in fig. 5.11, however the peak moves longer without developing a too pronounced shoulder, which is probably due to the faster heating rate of $280\,\mathrm{K\,h^{-1}}$ compared to $100\,\mathrm{K\,h^{-1}}$ for fig. 5.5. On the other hand, it might also be related to the pressure difference of the two samples of 12 bar, delaying the development of the shoulder for the higher pressure case.

As expected, the retention of the CO_2 was stronger in the case of 13 bar compared to 1 bar, only releasing the majority of the CO_2 at 323 K, compared to at 263 K for 1 bar. Due to the rapid temperature increase in these measurements, the precision of the release temperature is less than compared to doing it in smaller steps, as the sample does not get time to equilibriate at one temperature. Thus, these release temperatures should be treated as estimates instead of hard boundaries. For the development of the basal spacing of the two heating processes, the same behaviors are apparent. This demonstrates that the manner of heating (continuous or stepwise) is important for the dynamics. For the intensity there seems to be a linear increase for the case of 1 bar. This is not observed at 13 bar, as the temperature needed to release the CO_2 was high, yielding little space for the temperature to increase further, which might have caused the same linear behavior.

In general, the swelling of the NiFh clay investigated here is slightly larger than the expansion reported in ref.[23] of 12.19 Å, but the spacings are still comparable. The largest basal spacing at one layer of CO_2 was found to be 12.43 Å, and appears in fig. 5.7. Due to difficulties drying that sample, water was still present as it was exposed to CO_2. A mix of water and CO_2 in the clay have previously been shown to enhance the uptake of CO_2 in a sub-1WL state, and might also be the reason for the larger basal spacing [22, 65].

The objective of the measurement done at 253 K and up to 26 bar in fig. 5.7 was to see whether a hydration state corresponding to two layers of CO_2, as observed by Michels et al. [23] for Corning Inc. fluorohectorite, could also be observed in the clay produced by Prof. Josef Breu's group [44]. Unlike the results in ref.[23], no signs of a two-layer CO_2 state was observed, despite increasing the pressure further and reducing the temperature. Evidently, there is no change in the sample as the CO_2 enters the liquid phase, which is as expected as the full intercalation of CO_2 had already occurred, and no further intercalation states seem possible. It would be interesting to study whether the intercalation dynamics are different for dry clay exposed directly to liquid CO_2, compared to the gas phase.

6.2 Lithium-fluorohectorite

As for the studies performed by Cavalcanti et al. and Michels et al. [23, 26], the Lithium-fluorohectorite used here also swells in contact with CO_2. On the other hand, the intercalation is much faster under the same conditions of 20 bar and 253 K for the Bayreuth clay. Such a rapid intercalation was also observed for the NiFh, suggesting that a more homogeneous charge distribution in the clay promotes intercalation. In addition to intercalating CO_2 faster, the clay also releases the CO_2 at a lower temperature of $\approx$ 268 K, compared to the 308 K reported in ref.[23]. The lower release temperature is a rather undesirable property considering CO_2 storage, as it would be beneficial to have a high retention of the CO_2 to prevent leakage. Yet, a lower release temperature might be advantageous in other contexts, such as using LiFh in membranes, resulting in an easier cleaning process.

6.3 Effect of cation size and charge on the intercalation of CO_2

Of all the different clays, the the clay with the two smallest cations, Ni^{2+} and Li^{+}, and NaFh showed intercalation of CO_2. This result is unexpected in terms of the size of the cations, as it has been proposed that clays with small cations should not be able to incorporate CO_2 into the interlayer [25]. Conversely, ions of larger ionic radii should thereby readily absorb CO_2, which has not been observed for neither Cesium-fluorohectorite or Barium-fluorohectorite, which are by far the largest cations probed in this work. The belief is that larger cations in the clay will provide a larger basal spacing, and thus lower the energy barrier for intercalation [25, 42, 72]. In contrast to this, the basal spacing measured for the dehydrated clays, found in table 3, shows that the basal spacing of the larger cations are comparable to the basal spacings of the other cations. Interestingly, it is the cation of the smallest ionic radius that exhibits the largest basal spacing, and the Na^{+} cation of medium size exhibits the lowest basal spacing of all the probed clays. The reason for the large spacing in NiFh is unknown, but it has been proposed that it might be due to a Nickel-hydroxide, $Ni(OH)_2$ or possibly $(NiOH)^{+}$, in the interlayer [17]. Experiments to investigate this would be very useful in analyzing the intercalation dynamics of the CO_2, as other mechanisms/interactions might then be responsible for the large uptake of CO_2 by Nickel-fluorohectorite [26].

Experiments performed on NaFh have previously shown a very slow intercalation ($\sim$days) of CO_2 [24, 23]. The results of NaFh here also show a tiny peak at 12.2 Å, similar to the reported 12.4 Å in ref.[23]. The peak appears at 20 bar and 253 K, and is still present at 50 bar and 253 K, but appears to be receding. The apparent receding of the peak may be due to increased absorption of X-rays, which could decrease the intensity of this peak, so that it is partly hidden by the background scattering. However, whether the peak appears due to intercalation of H_2O or CO_2 cannot be determined. Further studies should re-investigate the NaFh sample at similar pressure and temperature over a longer period of time (days) to establish whether NaFh intercalates CO_2.

The lack of swelling in CsFh is surprising as it has been observed previously in Cesium-hectorite by both Bowers et al. [42] and Loganathan et al. [25]. On the other hand, the experimental conditions are very different in our case, as well as a different type of clay, which might be responsible for the absence of expansion. The large difference in experimental conditions and the difference in clay composition may also be the reason for the discrepancy between the results of other clays in this work and the ones presented in refs.[25, 42].

As clays with different cations show vastly different intercalation dynamics, it is evident that the type of cation is crucial. From the results in this work it cannot be seen that charge of the cation influence the swelling noticeably, as the swelling observed for both LiFh and NiFh was quite similar. That said, the charge does have implications for the amount of CO_2 absorbed by the clay [26]. As a larger charge on the cation requires less cations in the interlayer to compensate for the charge on the clay platelets, there is more room for CO_2 between the clay sheets. Other parameters that influence the intercalation is the ability of the cation

to polarize the CO_2 molecules, where a stronger polarization will lead to a stronger interaction between the cation and the CO_2. As CO_2 is a weakly/non-polar molecule, its interaction with the cation has been shown to be less important than the interaction between cation and clay [72]. Thus the charge of the clay platelets and the charge distribution may also have an impact on the energy barrier for intercalation.

7 Conclusion

7.1 Concluding remarks

Absorption and retention of CO_2 in fluorohectorite clay has been investigated with X-ray diffraction at two different synchrotron facilities. The results showed that the the two clays Nickel-fluorohectorite and Lithium-fluorohectorite readily absorb CO_2 at different conditions, and that NaFh shows signs of intercalating CO_2 as well. On the other hand, clays containing the cations Cs^+, Ba^{2+} and Ca^{2+} did not appear to intercalate CO_2 at any of the probed conditions. All experiments were performed on dry samples, or partially dry samples.

NiFh displayed slight swelling already at a pressure of 2 bar and a temperature of 300 K. However, the transition from dry to one layer of CO_2 intercalated was first initiated at 10 bar, and took place as pressure was increased to 12 bar. The final intercalation state displayed a basal spacing of 12.29 Å, compared to the dry state of 11.40 Å.

Similarly, the decrease in temperature from 300 K to 203 K at 1 bar induced an expansion of the NiFh at a temperature of 233 K. The resulting basal spacing was measured to be 12.32 Å. In addition, the retention of CO_2 was observed as the temperature was increased from 203 K to 400 K at 1 bar, retaining the CO_2 beyond the conditions for intercalation. The release of the CO_2 was first detected around 263 K, roughly 30 K higher than the temperature for intercalation.

It was also studied whether the phase of the CO_2 had any influence on the intercalation. After the transition to one layer of CO_2 intercalated, the conditions were changed so that the CO_2 entered the liquid phase. However, there was no indication that the NiFh clay absorbed more CO_2 or changed in any way at different conditions in the liquid phase. Lastly, the retention of CO_2 in NiFh at a pressure of 13 bar was investigated. As expected the temperature of release proved to be much higher than for the 1 bar case. The release temperature was found to be approximately 323 K.

For the LiFh, as well as the other cations, the critical pressure and temperature for intercalation was not investigated. Instead, the dry clays were exposed directly to 20 bar at 253 K to see if any intercalation was observed. Pressure was then further increased to 50 bar before being reduced to 1 bar and exposed to heating to examine the eventual retention properties. LiFh absorbed CO_2, and this happened immediately as it was exposed to 20 bar of CO_2. However, even at 50 bar a shoulder indicating that not all grains had intercalated CO_2 was visible. During the heating, the release started at 268 K. NaFh showed a minor peak at 12.2 Å at 20 and 50 bar at 253 K.

The other cations, surprisingly, did not intercalate CO_2. This result was unexpected due to the fact that absorption has previously been observed for similar clays under different conditions. Also, it was believed that clays of larger cations would more easily absorb CO_2 as they would prop open the interlayer for the CO_2 molecules. However, the results obtained in this work show no unambiguous tendency that larger basal spacings or higher cation charge results in intercalation.

7.2 Further studies and outlook

As NiFh shows the most promising results for CO_2 absorption, further studies should focus on this material. Investigation of dry NiFh should be conducted to identify the origin of the large basal spacing for this small ion. This may be done utilizing spectroscopic methods, which could convey information about whether other unknown components are present in the clay. Spectroscopy of NiFh with one layer of CO_2 intercalated would also be interesting, and provide valuable information on the orientations and organization of CO_2 within the layers and on the clay surface.

Additionally, measurements of the intercalation of CO_2 in NiFh over longer periods of time than those performed in this work should be conducted to verify whether an intercalation state of two CO_2 layers exists or not. Moreover, experiments that investigate the intercalation dynamics of NiFh directly exposed to liquid CO_2 could also be interesting. However, experimental details of such an experiment may prove challenging. The NaFh sample should also be investigated further to determine whether it intercalates CO_2 over longer periods of time.

Considering the clays of different cations, the results gave no clear answers regarding the relation between the size and charge of the cation to the intercalation of CO_2 into the clay. Therefore, more measurements and possibly simulations should be performed to get a clear overview of the influence that the type of cation has on the intercalation dynamics.

In the context of CO_2 capture and storage, the swelling of the clays is promising for storing larger amounts of CO_2 in geological storage sites. The absorbing and retention properties of the clay may also be especially suited for use as adsorbent material in industrial capture of CO_2, as the process of removing the CO_2 from the clay for transport would not require vast amounts of energy. Understanding the fundamental interactions and driving forces of the intercalation makes it easier to identify the uses clay can be put to. It also benefits future processes of enhancing the desired properties by for example functionalization of the clay.

A Calcium-fluorohectorite

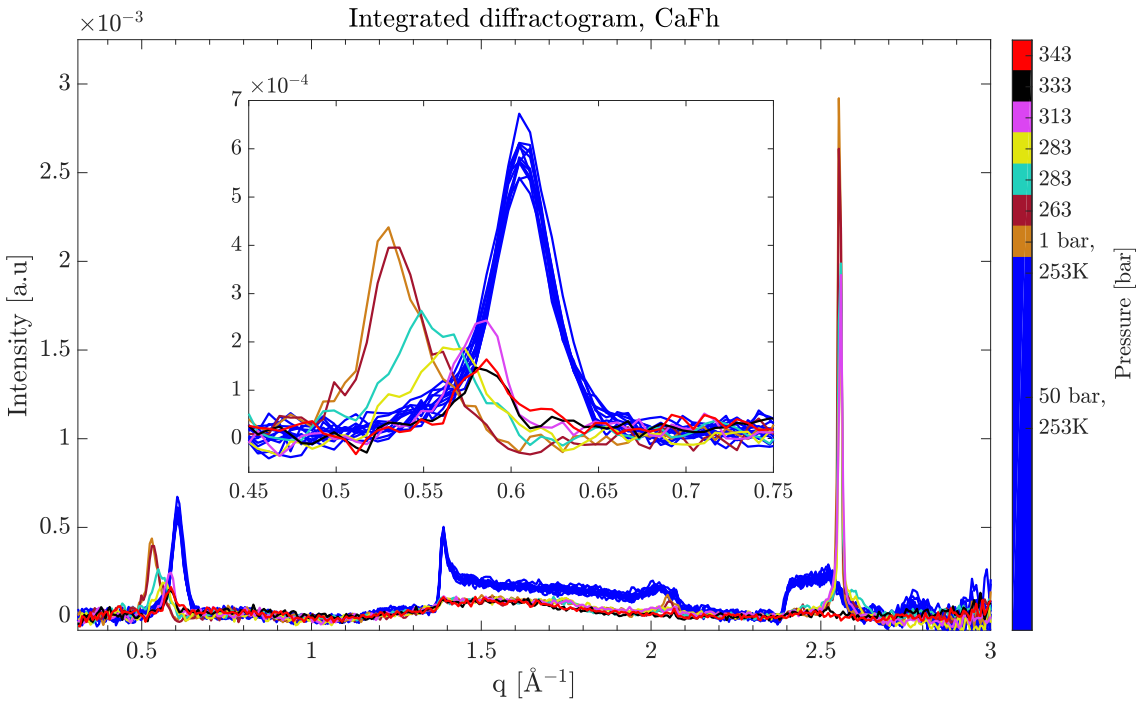

Figure A.1: Integrated diffractogram of CaFh heated from 253 K to 353 K at 1 bar. The color bar shows the temperature represented by each color, and also the pressure for 50 bar and 1 bar. The inset is a zoom in on the 001-Bragg peak.

As the pressure is decreased to 1 bar for CaFh, the 001 Bragg peak in fig. A.1 leaps to a lower q value of 0.523 $Å^{-1}$ (12.0 Å). This corresponds to the expansion one layer of water or CO_2 would produce. This change in basal spacing is not the only change. A very large peak, more than three times more intense than the 001 Bragg peak, also appears around 2.55 $Å^{-1}$. The peaks at lower and higher q values of the large peak have disappeared or are indistinguishable. As the temperature was increased however, the 001 Bragg peak moved back towards its original position. As it moves it becomes harder to distinguish it from the background. Simultaneously the large peak around 2.55 $Å^{-1}$ disappears between a temperature of 313 K and 333 K.

The jump of the 001 Bragg peak to a higher q value is very unexpected, and per now the observed movement of the 001 Bragg peak and the appearance of the larger peak at 2.55 $Å^{-1}$ cannot be explained. New measurements of this sample is advised to see if the result is repeatable or is due to an artifact or impurity of any kind.

References

[1] Stephen J Mojzsis. "Life and the Evolution of Earth's Atmosphere". In: *Earth inside and out* (2001), pp. 32–39.

[2] Martyn P. Chipperfield et al. "Detecting recovery of the stratospheric ozone layer". In: *Nature* 549 (Sept. 2017). Review Article, p. 211.

[3] *Greenhouse Gases and Clay Minerals: Enlightening Down-to-Earth Road Map to Basic Science of Clay-Greenhouse Gas Interfaces*. eng. Green Energy and Technology. Cham: Springer International Publishing, 2018.

[4] James Hansen, Makiko Sato, and Reto Ruedy. "Perception of climate change". In: *Proceedings of the National Academy of Sciences* (2012). eprint: `https://www.pnas.org/content/early/2012/07/30/1205276109.full.pdf`.

[5] Brage B Hansen et al. "Warmer and wetter winters: characteristics and implications of an extreme weather event in the High Arctic". In: *Environmental Research Letters* 9.11 (2014).

[6] Wei Shi et al. "Ocean acidification increases cadmium accumulation in marine bivalves: a potential threat to seafood safety". In: *Scientific Reports* 6 (Jan. 2016). Article, p. 20197.

[7] Jason M. Hall-Spencer et al. "Volcanic carbon dioxide vents show ecosystem effects of ocean acidification". In: *Nature* 454 (June 2008), p. 96.

[8] Terry L. Root et al. "Fingerprints of global warming on wild animals and plants". In: *Nature* 421 (Jan. 2003), p. 57.

[9] Joern Fischer et al. "Human behavior and sustainability". In: *Frontiers in Ecology and the Environment* 10.3 (2012), pp. 153–160.

[10] Munir A Hanjra and M Ejaz Qureshi. "Global water crisis and future food security in an era of climate change". In: *Food policy* 35.5 (2010), pp. 365–377.

[11] Nathan Stegall. "Designing for sustainability: A philosophy for ecologically intentional design". In: *Design Issues* 22.2 (2006), pp. 56–63.

[12] Dennis Y.C. Leung, Giorgio Caramanna, and M. Mercedes Maroto-Valer. "An overview of current status of carbon dioxide capture and storage technologies". In: *Renewable and Sustainable Energy Reviews* 39 (2014), pp. 426–443.

[13] A. Busch et al. "On sorption and swelling of CO2 in clays". In: *Geomechanics and Geophysics for Geo-Energy and Geo-Resources* 2.2 (June 2016), pp. 111–130.

[14] Guillaume Defontaine et al. "Nanoporous polymer–clay hybrid membranes for gas separation". In: *Journal of colloid and interface science* 343.2 (2010), pp. 622–627.

[15] AK Zulhairun et al. "Asymmetric mixed matrix membrane incorporating organically modified clay particle for gas separation". In: *Chemical Engineering Journal* 241 (2014), pp. 495–503.

[16] SA Hashemifard, AF Ismail, and T Matsuura. "Effects of montmorillonite nano-clay fillers on PEI mixed matrix membrane for CO2 removal". In: *Chemical Engineering Journal* 170.1 (2011), pp. 316–325.

[17] M.A.S. Altoé et al. "Continuous water adsorption states promoted by Ni2+ confined in a synthetic smectite". In: *Applied Clay Science* 123 (2016), pp. 83–91.

[18] Kenji Tamura, Hirohisa Yamada, and Hiromoto Nakazawa. "Stepwise hydration of high-quality synthetic smectite with various cations". In: *Clays and Clay Minerals* 48.3 (2000), pp. 400–404.

[19] GJ Da Silva et al. "Synchrotron x-ray scattering studies of water intercalation in a layered synthetic silicate". In: *Physical Review E* 66.1 (2002), p. 011303.

[20] Elisabeth Lindbo Hansen et al. "Swelling transition of a clay induced by heating". In: *Scientific reports* 2 (2012), p. 618.

[21] Leander Michels et al. “EXAFS and XRD studies in synthetic Ni-fluorohectorite”. In: *Applied Clay Science* 96 (2014), pp. 60–66.

[22] Herbert T Schaef et al. “Competitive sorption of CO2 and H2O in 2: 1 layer phyllosilicates”. In: *Geochimica et Cosmochimica Acta* 161 (2015), pp. 248–257.

[23] Leander Michels et al. “Intercalation and Retention of Carbon Dioxide in a Smectite Clay promoted by Interlayer Cations”. In: *Scientific Reports* 5 (Mar. 2015), pp. 1–9.

[24] Henrik Hemmen et al. “X-ray studies of carbon dioxide intercalation in Na-fluorohectorite clay at near-ambient conditions”. In: *Langmuir* 28.3 (2012), pp. 1678–1682.

[25] Narasimhan Loganathan et al. “Clay Swelling in Dry Supercritical Carbon Dioxide: Effects of Interlayer Cations on the Structure, Dynamics, and Energetics of CO2 Intercalation Probed by XRD, NMR, and GCMD Simulations”. In: *The Journal of Physical Chemistry C* 122.8 (2018), pp. 4391–4402.

[26] Leide P Cavalcanti et al. “A nano-silicate material with exceptional capacity for CO 2 capture and storage at room temperature”. In: *Scientific reports* 8.1 (2018), p. 11827.

[27] F. Bergaya and G. Lagaly. *General introduction: Clays, clay minerals, and clay science*. 1st ed. Vol. 5. Elsevier Inc., 2013, pp. 1–19.

[28] Jemima Daniela Dias Moraes et al. “Clay minerals: Properties and applications to dermocosmetic products and perspectives of natural raw materials for therapeutic purposes—A review”. In: *International Journal of Pharmaceutics* 534.1 (2017), pp. 213–219.

[29] Sin-Ying Tan et al. “Nano-mechanical properties of clay-armoured emulsion droplets”. In: *Soft Matter* 8.11 (2012), pp. 3112–3121.

[30] Azarmidokht Gholamipour-Shirazi, Marcio S Carvalho, and Jon Otto Fossum. “Controlled microfluidic emulsification of oil in a clay nanofluid: Role of salt for Pickering stabilization”. In: *The European Physical Journal Special Topics* 225.4 (2016), pp. 757–765.

[31] Neal S. Eash et al. *Soil Science Simplified*. Wiley-Blackwell, 2015.

[32] J Abdo and MD Haneef. “Clay nanoparticles modified drilling fluids for drilling of deep hydrocarbon wells”. In: *Applied Clay Science* 86 (2013), pp. 76–82.

[33] Johannes M DeBeer. *Drilling mud additive*. US Patent 5,401,719. Mar. 1995.

[34] George R. Gray and H.C.H. Darley. *Composition and Properties of Oil Well Drilling Fluids (4th Edition)*. Elsevier, 1980.

[35] Jay P Deville, Brady Fritz, Michael Jarrett, et al. “Development of water-based drilling fluids customized for shale reservoirs”. In: *SPE Drilling & Completion* 26.04 (2011), pp. 484–491.

[36] Lena Moren. *Design and production of the KBS-3 repository*. Tech. rep. Swedish Nuclear Fuel and Waste Management Co., 2010.

[37] M.F. Brigatti, E. Galán, and B.K.G. Theng. “Chapter 2 - Structure and Mineralogy of Clay Minerals”. In: *Handbook of Clay Science*. Ed. by Faïza Bergaya and Gerhard Lagaly. Vol. 5. Developments in Clay Science. Elsevier, 2013, pp. 21–81.

[38] O Yu Golubeva, EN Korytkova, and VV Gusarov. “Hydrothermal synthesis of magnesium silicate montmorillonite for polymer-clay nanocomposites”. In: *Russian journal of applied chemistry* 78.1 (2005), pp. 26–32.

[39] I. Bibi et al. “Chapter 21 - Clay Minerals: Structure, Chemistry, and Significance in Contaminated Environments and Geological CO2 Sequestration”. In: *Environmental Materials and Waste*. Ed. by M.N.V. Prasad and Kaimin Shih. Academic Press, 2016, pp. 543–567.

[40] B.K.G. Theng. “Chapter 1 - The Clay Minerals”. In: *Formation and Properties of Clay-Polymer Complexes*. Ed. by B.K.G. Theng. Vol. 4. Developments in Clay Science. Elsevier, 2012, pp. 3–45.

[41] X. Ma, W.J. Bruckard, and R. Holmes. “Effect of collector, pH and ionic strength on the cationic flotation of kaolinite”. In: *International Journal of Mineral Processing* 93.1 (2009), pp. 54–58.

[42] Geoffrey M. Bowers et al. "Role of Cations in CO2 Adsorption, Dynamics, and Hydration in Smectite Clays under in Situ Supercritical CO2 Conditions". In: *The Journal of Physical Chemistry C* 121.1 (Jan. 2017), pp. 577–592.

[43] Sabine Rosenfeldt et al. "In-Depth Insights into the Key Steps of Delamination of Charged 2D Nanomaterials". In: *Langmuir* 32.41 (Oct. 2016), pp. 10582–10588.

[44] Josef Breu et al. "Charge homogeneity in synthetic fluorohectorite". In: *Chemistry of Materials* 13.11 (2001), pp. 4213–4220.

[45] John Meurig Thomas. "The birth of X-ray crystallography". In: *Nature* 491 (Nov. 2012). Comment, p. 186.

[46] D. A. Hall et al. "A high energy synchrotron x-ray study of crystallographic texture and lattice strain in soft lead zirconate titanate ceramics". In: *Journal of Applied Physics* 96.8 (2004), pp. 4245–4252. eprint: `https://doi.org/10.1063/1.1787590`.

[47] "Quantitative Analysis". In: *Two-Dimensional X-Ray Diffraction*. John Wiley & Sons, Ltd, 2009. Chap. 12, pp. 369–392. eprint: `https://onlinelibrary.wiley.com/doi/pdf/10.1002/9780470502648.ch12`.

[48] E. DiMasi et al. "Orientational order in gravity dispersed clay colloids: A synchrotron x-ray scattering study of Na fluorohectorite suspensions". In: *Phys. Rev. E* 64 (6 Nov. 2001), p. 061704.

[49] Marco Linari et al. "Force generation by skeletal muscle is controlled by mechanosensing in myosin filaments". In: *Nature* 528.7581 (2015), pp. 276–279.

[50] Charles Kittel. *Introduction to solid state physics*. eng. 8th ed. Hoboken, N.J: Wiley, 2005.

[51] T. Zemb and P. Lindner. *Neutrons, X-rays and Light: Scattering Methods Applied to Soft Condensed Matter*. North-Holland delta series. Elsevier, 2002.

[52] Philip Hofmann. *Solid state physics : an introduction (Physics textbook) / Philip Hofmann*. eng. 2nd ed. Weinheim: Wiley-VCH, 2015.

[53] J Als-Nielsen. *Elements of modern X-ray physics*. eng. New York: Wiley, 2001.

[54] Antonella Balerna and Settimio Mobilio. "Introduction to Synchrotron Radiation". In: *Synchrotron Radiation: Basics, Methods and Applications*. Ed. by Settimio Mobilio, Federico Boscherini, and Carlo Meneghini. Berlin, Heidelberg: Springer Berlin Heidelberg, 2015, pp. 3–28.

[55] European Synchrotron Radiation Facility. *TOP-UP*. `https://www.esrf.eu/home/UsersAndScience/Accelerators/Operation/top-up.html`, Last accessed on 2019-05-09.

[56] Brazilian Synchrotron Light Laboratory. *ACCELERATORS*. `https://www.lnls.cnpem.br/uvx-en/accelerators/`, Last accessed on 2019-05-09.

[57] Torben R Jensen et al. "Versatile in situ powder X-ray diffraction cells for solid–gas investigations". In: *Journal of applied crystallography* 43.6 (2010), pp. 1456–1463.

[58] Hilgenberg. *MARK-TUBES MADE OF BOROSILICATE GLASS*. `https://www.hilgenberg-gmbh.de/en/catalog/test-tubes/mark-tubes/detail/?tt_products%5BbackPID%5D=158&tt_products%5Bproduct%5D=32&cHash=`, Last accessed on 2019-05-09.

[59] Brian Richard Pauw. "Everything SAXS: small-angle scattering pattern collection and correction". In: *Journal of Physics: Condensed Matter* 25.38 (2013), p. 383201.

[60] Brian Richard Pauw et al. "The modular small-angle X-ray scattering data correction sequence". In: *Journal of applied crystallography* 50.6 (2017), pp. 1800–1811.

[61] Vadim Dyadkin et al. "A new multipurpose diffractometer PILATUS@SNBL". In: *Journal of Synchrotron Radiation* 23.3 (May 2016), pp. 825–829.

[62] J. Filik et al. "Processing two-dimensional X-ray diffraction and small-angle scattering data in *DAWN 2*". In: *Journal of Applied Crystallography* 50.3 (June 2017), pp. 959–966.

[63] Raymond Chang. *General chemistry : the essential concepts*. eng. 7th ed., International ed. New York: McGraw-Hill, 2014.

[64] Joshua Halpern. *8.2: Atomic and Ionic Radius*. https://chem.libretexts.org/Courses/Bellarmine_University/BU%3A_Chem_103_(Christianson)/Phase_3%3A_Atoms_and_Molecules_-_the_Underlying_Reality/8%3A_Periodic_Trends_in_Elements_and_Compounds/8.2%3A_Atomic_and_Ionic_Radius, Last accessed on 2019-05-10.

[65] John S Loring et al. "In situ study of CO2 and H2O partitioning between Na–montmorillonite and variably wet supercritical carbon dioxide". In: *Langmuir* 30.21 (2014), pp. 6120–6128.

[66] Sterling Hendricks and Edward Teller. "X-ray interference in partially ordered layer lattices". In: *The Journal of Chemical Physics* 10.3 (1942), pp. 147–167.

[67] Randall T Cygan, Vyacheslav N Romanov, and Evgeniy M Myshakin. "Molecular simulation of carbon dioxide capture by montmorillonite using an accurate and flexible force field". In: *The Journal of Physical Chemistry C* 116.24 (2012), pp. 13079–13091.

[68] Mohan Maruthi Sena et al. "Supercritical carbon dioxide at smectite mineral–water interfaces: Molecular dynamics and adaptive biasing force investigation of CO2/H2O mixtures nanoconfined in Na-montmorillonite". In: *Chemistry of Materials* 27.20 (2015), pp. 6946–6959.

[69] H. Hemmen et al. "X-ray studies of interlayer water absorption and mesoporous water transport in a weakly hydrated clay". In: *Phys. Rev. E* 82 (3 Sept. 2010), p. 036315.

[70] Jon Otto Fossum. Personal communication, 10.05.19.

[71] LE Michels et al. "Synchrotron x-ray scattering studies of Lifluorohectorite synthetic clay: Random intercalation states". In: *Proceedings of 2nd International Workshop on Complex Physical Phenomena in Materials*. complexphysics. org. 2012, pp. 31–34.

[72] Herbert T Schaef et al. "Tipping point for expansion of layered aluminosilicates in weakly polar solvents: Supercritical CO2". In: *ACS applied materials & interfaces* 9.42 (2017), pp. 36783–36791.

[73] JJ Fripiat et al. "Interlamellar adsorption of carbon dioxide by smectites". In: *Clays and Clay Minerals* 22.1 (1974), pp. 23–30.

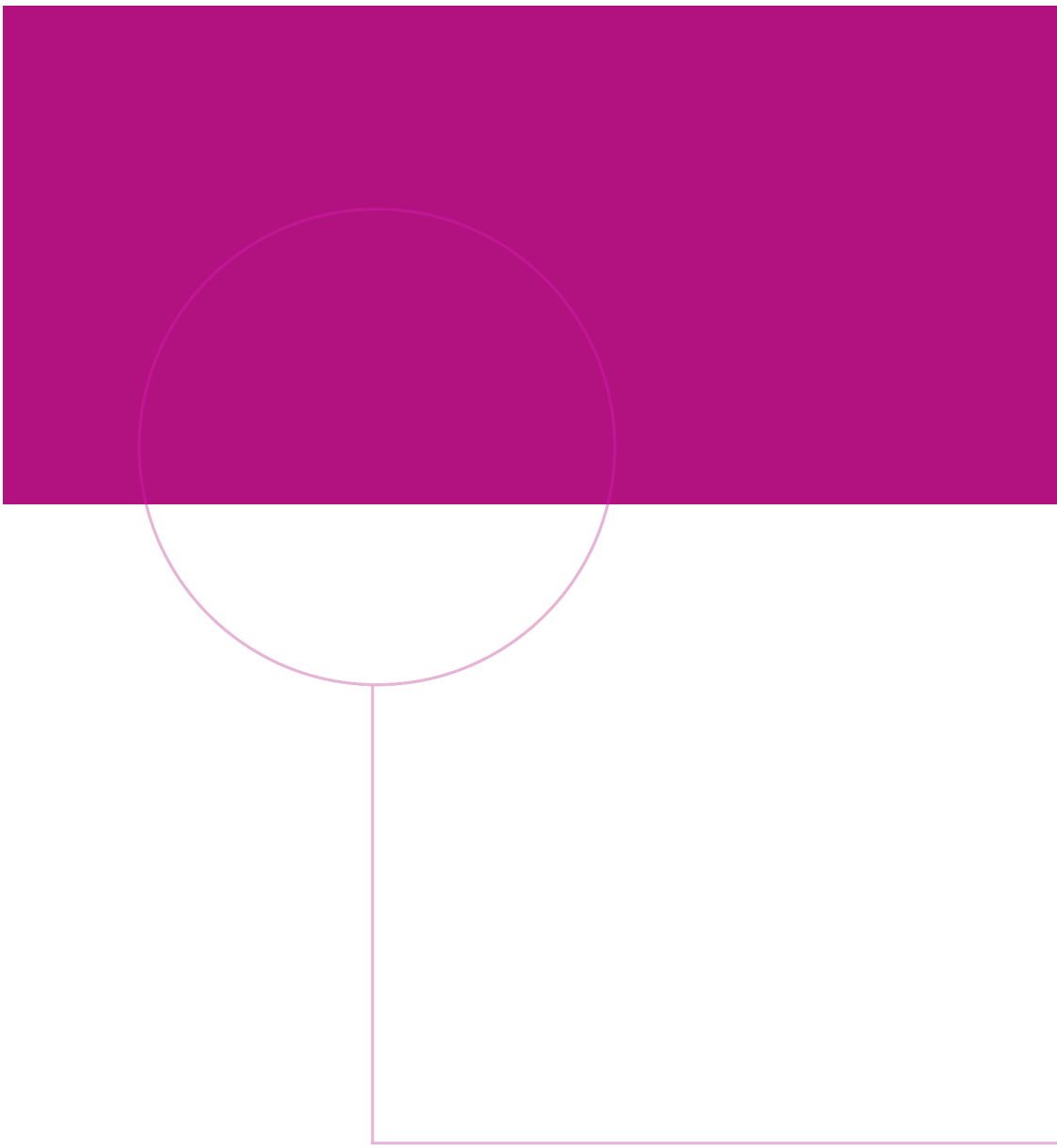

NTNU

Norwegian University of
Science and Technology